machines

MDPI

Article

An Improved Adaptive Sliding Mode Control Approach for Anti-Slip Regulation of Electric Vehicles Based on Optimal Slip Ratio

Houzhong Zhang, Yiyun Qi *, Weijian Si and Chengyin Zhang

Automotive Engineering Research Institute, Jiangsu University, Zhenjiang 212013, China; 1000004025@ujs.edu.cn (H.Z.); 2222338051@stmail.ujs.edu.cn (W.S.); 2212104005@stmail.ujs.edu.cn (C.Z.)
* Correspondence: 2212204027@stmail.ujs.edu.cn

Abstract: To optimize the acceleration performance of independently driven electric vehicles with four in-wheel motors, this paper proposes an anti-slip regulation (ASR) strategy based on dynamic road surface observer for more efficient tracking of the optimal slip ratio and enhanced vehicle acceleration. The method uses the Unscented Kalman Filter (UKF) observer to estimate vehicle speed and calculate the actual slip ratio, while a fuzzy controller based on the Burckhardt tire model identifies road surfaces. The road's peak adhesion coefficient and optimal slip ratio curve are fitted using a Back Propagation Neural Network (BPNN) optimized by Particle Swarm Optimization (PSO). The control strategy further refines torque management through an adaptive sliding mode control (ASMC) that integrates adaptive laws and a super-twisting sliding mode approach to track the optimal slip ratio. Joint simulations with MATLAB/Simulink and Carsim on low-adhesion, joint, and split road surfaces demonstrate that the strategy quickly and accurately identifies the optimal slip ratio across various road surfaces. This enables the tire slip ratio to approach the optimal value in minimal time, significantly improving vehicle dynamic performance. Compared to conventional sliding mode controllers, the optimized ASMC reduces chattering and improves control precision.

Keywords: electric vehicle with in-wheel motors; vehicle speed estimation; road surface observer; fuzzy control; optimal slip ratio; adaptive sliding mode control

check for updates

Citation: Zhang, H.; Qi, Y.; Si, W.; Zhang, C. An Improved Adaptive Sliding Mode Control Approach for Anti-Slip Regulation of Electric Vehicles Based on Optimal Slip Ratio. *Machines* **2024**, *12*, 769. https://doi.org/10.3390/machines12110769

Academic Editor: Dan Zhang

Received: 14 October 2024
Revised: 25 October 2024
Accepted: 31 October 2024
Published: 31 October 2024

Copyright: © 2024 by the authors. Licensee MDPI, Basel, Switzerland. This article is an open access article distributed under the terms and conditions of the Creative Commons Attribution (CC BY) license (https://creativecommons.org/licenses/by/4.0/).

1. Introduction

With worsening global pollution, reducing fossil fuel emissions and finding alternative energy sources have become key goals in the automotive industry. Electric vehicles, favored for their low emissions and high efficiency, are gaining increased attention [1,2]. In recent years, electric vehicle performance and efficiency have improved, with drive-by-wire chassis and distributed drive widely adopted. Four-wheel independent drive technology, valued for its handling, power, and road adaptability, is gaining more attention [3,4]. Electric vehicles with four in-wheel motors do not require traditional transmission structures, as each wheel is directly driven by its motor. These motors are typically permanent magnet synchronous motors, known for their high power factor and high starting torque, giving four-wheel independent drive electric vehicles superior power performance [5,6]. Under an effective control strategy, both longitudinal and lateral control of distributed drive vehicles can be significantly enhanced. For example, selecting an optimal control architecture can effectively improve the vehicle's lateral stability [7]. Additionally, control strategies can achieve more efficient energy-saving control, highlighting the flexibility of such systems [8]. Furthermore, there is still extensive research potential in the field of longitudinal control, particularly in drive control. By further optimizing drive control strategies, distributed drive vehicles are expected to make significant advancements in power performance, energy efficiency, and driving safety. This research is crucial for improving the overall performance of vehicles. Due to their strong power, four-wheel independent drive electric

vehicles can slip on low-traction surfaces, risking tire damage and potential safety hazards [9]. Therefore, traction control for electric vehicles with four in-wheel motors holds significant research value and importance.

Anti-slip regulation (ASR) plays a key role in vehicle performance and stability. In traditional vehicles, ASR technology is relatively mature, primarily achieved by limiting engine torque and coordinating with the braking system. However, this method has certain limitations [10]. Four-wheel independent drive electric vehicles rely on in-wheel motors, which offer faster response and more precise control, allowing for better monitoring of each wheel's slip condition. Compared to hydraulic and traditional mechanical systems, this setup enables more flexible and accurate traction control [11,12]. Figure 1 shows the structure of an electric vehicle with four in-wheel motors.

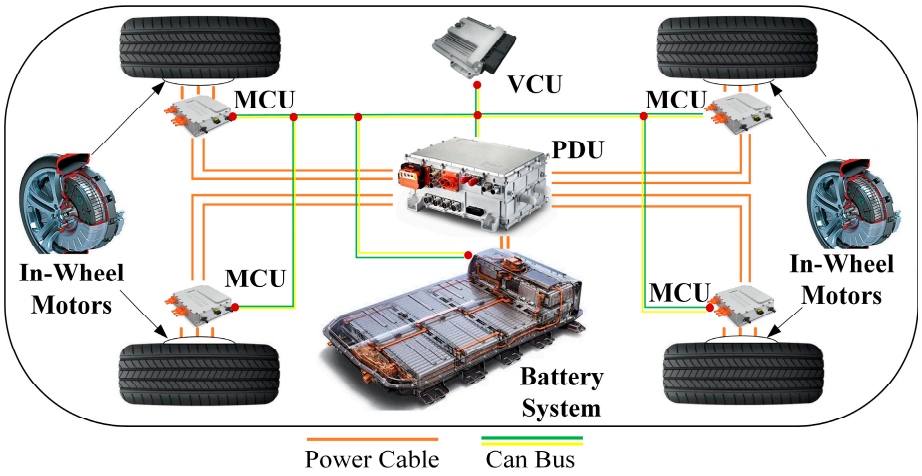

Figure 1. Typical structure of an electric vehicle with four in-wheel motors.

Due to varying research focuses, traction control strategies for fuel vehicles and electric vehicles have been widely developed. These methods are primarily classified into direct torque control and slip ratio control [13].

Direct torque control aims to limit wheel slip on low-traction surfaces by detecting wheel states such as angular acceleration, inertia, or friction slip derivatives, without relying on slip ratio. Hori and colleagues developed a traction control system (TCS) based on model-following control (MFC) and optimal slip ratio control, assuming that wheel inertia drops sharply during slip to achieve anti-slip control [14]. Yin, Hori, and Zhang proposed an ASR method based on direct torque output limitation, establishing a link between road traction and target slip ratio using wheel speed and feedback torque [15,16]. However, the MFC requires precise road friction information and is highly sensitive to changes in model parameters. Colli et al. used an adhesion estimator and an adhesion gradient controller, which can track the desired target over a large operating range under unknown road surfaces [17]. Joško, Danijel, and Gilberto improved the robustness of traction control against road surface changes through static curve gradient tire control and robust switching control, based on a bidirectional sawtooth excitation signal [18]. Zhang designed a TCS based on S-line control and a slope optimization algorithm using minimum steady-state fluctuation extremum seeking to ensure that the slip ratio approaches the optimal value [19].

Although torque-based control limits wheel slip, real-time estimation of maximum output torque on varying road surfaces is challenging. Chen et al. proposed a slip ratio-based control to improve acceleration, better suited for four-wheel independent drive electric vehicles [20]. The slip ratio-based control uses the optimal slip ratio as a key state to achieve precise torque management, combining dynamic models with control methods like PID, MPC, and sliding mode control. Yang, Li, and Fu set the target slip ratio at 0.15 to reduce urban driving slip and proposed an ASR method using PID and logic thresholds.

While PID control lacks robustness on varying road surfaces, fuzzy algorithms can improve this [21]. Li et al. applied sliding mode control combined with fuzzy algorithms for torque distribution among power sources, enhancing the handling stability of four-wheel-drive hybrid vehicles [22]. The MPC algorithm replaces global one-time optimization with a rolling optimization strategy, allowing for timely compensation of uncertainties and better dynamic performance. Sekour and Hartani proposed a direct torque control (DTC) algorithm based on nonlinear model predictive control (NMP) [23]. Sliding mode control (SMC) offers fast response and robustness to disturbances but suffers from oscillation. Zhou et al. reduced this by using a special switching function to slow the system near the sliding surface [24]. Ricardo et al. proposed a continuous SMC algorithm using continuous approximation, showing good slip regulation and robustness against disturbances [25]. Yu et al. designed a robust adaptive ASR controller that estimates the road peak adhesion coefficient using the Burckhard tire model and non-affine parameter estimation, improving acceleration by considering road surfaces [26]. Guo et al. designed a method to determine the optimal slip ratio based on road surface classification, adjusting torque output to keep the slip ratio near its optimal value [6].

In summary, the optimal slip ratio-based ASR controller includes optimal slip ratio identification and torque control. For electric vehicles with four in-wheel motors, the distributed drive offers greater optimization potential. This paper designs a road surface optimal slip ratio observer, estimating vertical and longitudinal forces using a seven-degree-of-freedom (7DOF) vehicle model and the Dugoff tire model. Fuzzy control and PSO-based BP neural networks are used to fit the optimal slip ratio curve. For torque control, an improved adaptive sliding mode control is adopted, improving the adaptive law and adjusting the sliding surface using the super-twisting sliding mode algorithm. This adjusts the hub motor torque, enhancing driving performance.

The structure of this paper is as follows: Section 2 establishes the 7DOF vehicle dynamics model and related models; Section 3 introduces the design of the overall control system, including the vehicle speed estimation method based on the UKF observer, an optimal slip ratio identification algorithm combined with the dynamic model, and an improved adaptive sliding mode control for optimal slip ratio tracking, achieving anti-slip regulation control; Section 4 conducts simulation tests, validating the effectiveness of the proposed methods through comparison; finally, Section 5 concludes the paper.

2. System Scheme

2.1. Vehicle Dynamics Model

The dynamic characteristics of a vehicle system are difficult to accurately describe with mathematical models. This is because many complex factors, such as mass distribution, suspension system, speed, and road conditions, interact with each other. These interactions cause nonlinearity and uncertainty, making it hard to model the system's behavior precisely. Additionally, different state parameters are linked in various directions (lateral, longitudinal, vertical), adding complexity and nonlinearity to the model. We use a seven-degree-of-freedom (7DOF) model because it not only meets our control needs but also provides a more accurate and robust prediction of vehicle behavior compared to simpler models like the 2DOF or 3DOF.

To establish a vehicle dynamics model, it is necessary to make certain reasonable assumptions about the vehicle model during the modeling process: 1. Assume a flat road surface, neglecting road gradient, air resistance, and vertical motion of the vehicle and wheels. 2. Assume the vehicle is symmetrical left and right, with the same roll center height at the front and rear; 3. Neglect the impact of suspension damping and disregard the axle load changes caused by vehicle pitch during acceleration; 4. Assume the rolling radii of the left and right wheels are identical. Based on the above assumptions, a seven-degree-of-freedom vehicle model is established, as shown in Figure 2.

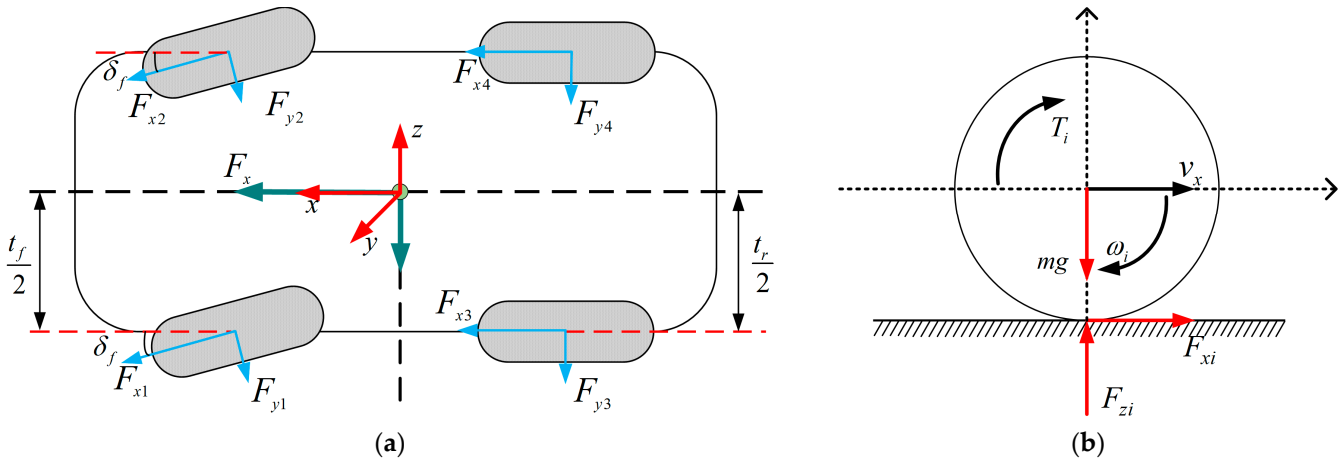

Figure 2. DOF vehicle dynamics model: (**a**) Vehicle body model; (**b**) Wheel model.

In our vehicle dynamics modeling, we have ignored the effects of road gradient, air resistance, and suspension damping. This is based on simulations under relatively flat road conditions and moderate speeds, focusing on the effectiveness of control strategies from a theoretical perspective. The simplified assumptions mainly affect real-world factors like road friction variation and suspension damping for road recognition, but they don't significantly interfere with the core logic of the control strategies. From a theoretical research standpoint, these assumptions are considered reasonably negligible.

There are longitudinal, lateral, and yaw motions of the vehicle, and the rotational motion of the four wheels [27]. Common longitudinal motion dynamics equations based on the seven-degree-of-freedom vehicle model:

$$m(\dot{v}_x - v_y\gamma) = (F_{x1} + F_{x2})\cos\delta - (F_{y1} + F_{y2})\sin\delta + F_{x3} + F_{x4} \tag{1}$$

Equations of lateral motion:

$$m(\dot{v}_y + v_x\gamma) = (F_{x1} + F_{x2})\sin\delta + (F_{y1} + F_{y2})\cos\delta + F_{y3} + F_{y4} \tag{2}$$

Equations of yaw motion:

$$I_z\dot{\gamma} = [(F_{x1} + F_{x2})\sin\delta + (F_{y1} + F_{y2})\cos\delta]A + [(F_{x2} - F_{x1})\cos\delta + (F_{y2} - F_{y1})\sin\delta]\frac{t_r}{2} + (F_{x4} - F_{x3})\frac{t_r}{2} - (F_{y3} + F_{y4})B \tag{3}$$

where m represents the total vehicle mass, v_x and v_y represent the longitudinal and lateral velocities, γ is the yaw rate of the vehicle, δ is the front wheel steering angle input, and F_{xi} and F_{yi} are the longitudinal and lateral tire forces, respectively (i = 1, 2, 3, 4 represent the left front (FL) wheel, right front (FR) wheel, left rear (RL) wheel, and right rear (RR) wheel); $L = A + B$, a and b represent the distances from the center of mass to the front and rear axles, respectively, t_f and t_r are the front and rear track widths, and I_z is the moment of inertia of the vehicle about the z-axis.

Since the focus of this paper is on longitudinal dynamics, there is no direct steering angle input, and the longitudinal equation can be simplified as follows:

$$m\dot{v}_x = F_{x1} + F_{x2} + F_{x3} + F_{x4} \tag{4}$$

Vertical loads on the four tires:

$$F_{z1} = mg\frac{B}{2L} - ma_x\frac{h}{2L} - ma_yB\frac{h}{Lt_f} \tag{5}$$

$$F_{z2} = mg\frac{B}{2L} - ma_x\frac{h}{2L} + ma_yB\frac{h}{Lt_f} \tag{6}$$

$$F_{z3} = mg\frac{A}{2L} + ma_x\frac{h}{2L} - ma_yA\frac{h}{Lt_r} \tag{7}$$

$$F_{z4} = mg\frac{A}{2L} + ma_x\frac{h}{2L} + ma_yA\frac{h}{Lt_r} \tag{8}$$

where F_{zi} represents the vertical loads on the four wheels, a_x is the longitudinal acceleration, a_y is the lateral acceleration, h is the height of the vehicle's center of gravity, and g is the gravitational acceleration. For ASR control, the forces on a single wheel model can largely reflect the vehicle's motion during acceleration, making it intuitive for modeling and analysis. The single-wheel dynamics model for four-wheel independent drive represents the basic longitudinal dynamics of the vehicle [28]. Since this paper does not focus on braking forces, only the single-wheel dynamics model in the driving state is considered, as shown in Figure 2b for the wheel dynamics model.

$$J\dot{\omega}_i = T_i - RF_{xi} \tag{9}$$

$$M\dot{v}_x = F_{xi} \tag{10}$$

where J represents the rotational inertia of the wheel, T_i is the corresponding wheel driving torque, R is the wheel rolling radius, and F_{xi} is the longitudinal reaction force from the ground. Since the vehicle is a four-wheel independent drive electric vehicle, M is 1/4 of the total vehicle mass.

The relationship between the longitudinal driving force of the driven wheels and the normal force is:

$$F_{xi} = \mu_i F_{zi} \tag{11}$$

where μ_i represents the utilization adhesion coefficient, and F_{zi} represents the normal reaction force from the ground.

The slip ratio is a critical state variable in longitudinal dynamics, effectively reflecting the relative state between the wheels and the road surface. Subsequent ASR controller utilizes this state variable to optimize the torque distribution among the four driven wheels based on the corresponding slip ratios, which can be expressed as follows:

$$\lambda_i = \begin{cases} \frac{\omega_i R - v_x}{\omega_i R}, Driving \\ \frac{v_x - \omega_i R}{v_x}, Braking \end{cases} \tag{12}$$

where λ_i represents the wheel slip ratio, v_x is the longitudinal vehicle speed, and ω_i indicate the angular velocity of the corresponding wheel. During vehicle propulsion and braking, there are two methods to calculate the slip ratio. This study primarily focuses on the longitudinal driving of the vehicle; therefore, the calculation method for slip ratio during acceleration is selected.

2.2. Dugoff Tire Model

In vehicle dynamics, tires are the only road contact point, directly affecting performance. Accurate modeling is essential. The Dugoff tire model simplifies the vertical pressure curve compared to the Pacejka and Shape models, allowing for independent lateral and longitudinal stiffness through combined force analysis [29]. The longitudinal and lateral forces of a tire are closely linked to the road's adhesion coefficient. The Dugoff tire model, as a steady-state model, assumes that the friction force arises from the combined effects of lateral and longitudinal forces. Its minimal parameter requirements make it well-suited for describing the nonlinear characteristics of tires [30]. The Dugoff tire model

offers a more accurate fit in the longitudinal direction, making it suitable for this study's conditions. Its calculation formula is as follows:

$$\begin{cases} F_{xi} = \mu_i F_{xi}^0 = \mu_i F_{zi} C_x \frac{\lambda_i}{1-\lambda_i} f(L) \\ F_{yi} = \mu_i F_{yi}^0 = \mu_i F_{zi} C_y \frac{\tan(a_i)}{1-\lambda_i} f(L) \end{cases} \tag{13}$$

$$f(L) = \begin{cases} L(2-L) & , L < 1 \\ 1 & , L \geq 1 \end{cases} \tag{14}$$

$$L = \frac{1}{\sqrt[2]{C_x^2 \lambda_i^2 + C_y^2 \tan^2 a}} (1-\lambda_i) \times (1 - \varepsilon v \sqrt{C_x^2 \lambda_i^2 + C_y^2 \tan^2 a}) \tag{15}$$

where C_x is the tire's longitudinal stiffness, C_y is the tire's lateral stiffness, a_i is the slip angle, ε is the velocity influence factor, and L is the tire's slip characteristics. The calculation formulas for the slip angles of each tire are as follows:

$$a_{1,2} = \delta - \arctan\left(\frac{v_y + A\gamma}{v_x \pm \frac{t_f \gamma}{2}}\right) \tag{16}$$

$$a_{3,4} = -\arctan\left(\frac{v_y - B\gamma}{v_x \pm \frac{t_r \gamma}{2}}\right) \tag{17}$$

Using the Dugoff tire model, the longitudinal forces of each tire can be obtained, enabling the identification of the road surface adhesion coefficient.

2.3. Driver Model

This paper's drive slip control system focuses on starting acceleration on surfaces with varying adhesion coefficients, with the driver model targeting only the longitudinal speed. The desired speed serves as the input, controlled by a torque PI controller that distributes torque to the four-wheel hub motors. The PI control equations for the driver model are as Equation (18):

$$T_{driver} = K_p e(t) + K_i \int_0^t e(t) dt \tag{18}$$

$$e(t) = v_{driver} - v_x \tag{19}$$

where K_p is the proportional gain, K_i is the integral gain, and v_{driver} is the desired vehicle speed.

2.4. Motor Model

Since this paper primarily investigates the application of in-wheel motors in ASR (Anti-Slip Regulation) control, a simplified second-order equivalent model is employed.

$$G(s) = \frac{T_{reqi}}{T_{outi}} = \frac{1}{1 + 2\xi s + 2\xi^2 s^2} \tag{20}$$

where T_{reqi} is the request torque for each in-wheel motor, T_{outi} is the output torque for each in-wheel motor, ξ is the damping ratio, $\xi = 0.006$, and s is the dynamic response time constant.

3. Design of Anti-Slip Regulation System

The anti-slip control for a four-wheel-drive electric vehicle based on road surface recognition focuses on managing hub drive using the optimal slip ratio. The actual slip ratio is obtained through the UKF observer vehicle speed estimator and wheel angular velocity measurements. The road surface observer, optimized with a fuzzy control algorithm, vehicle dynamics model, and Dugoff tire model, further refines the control. The target

torque output is achieved using an improved adaptive sliding mode control method. The overall control architecture is shown in Figure 3.

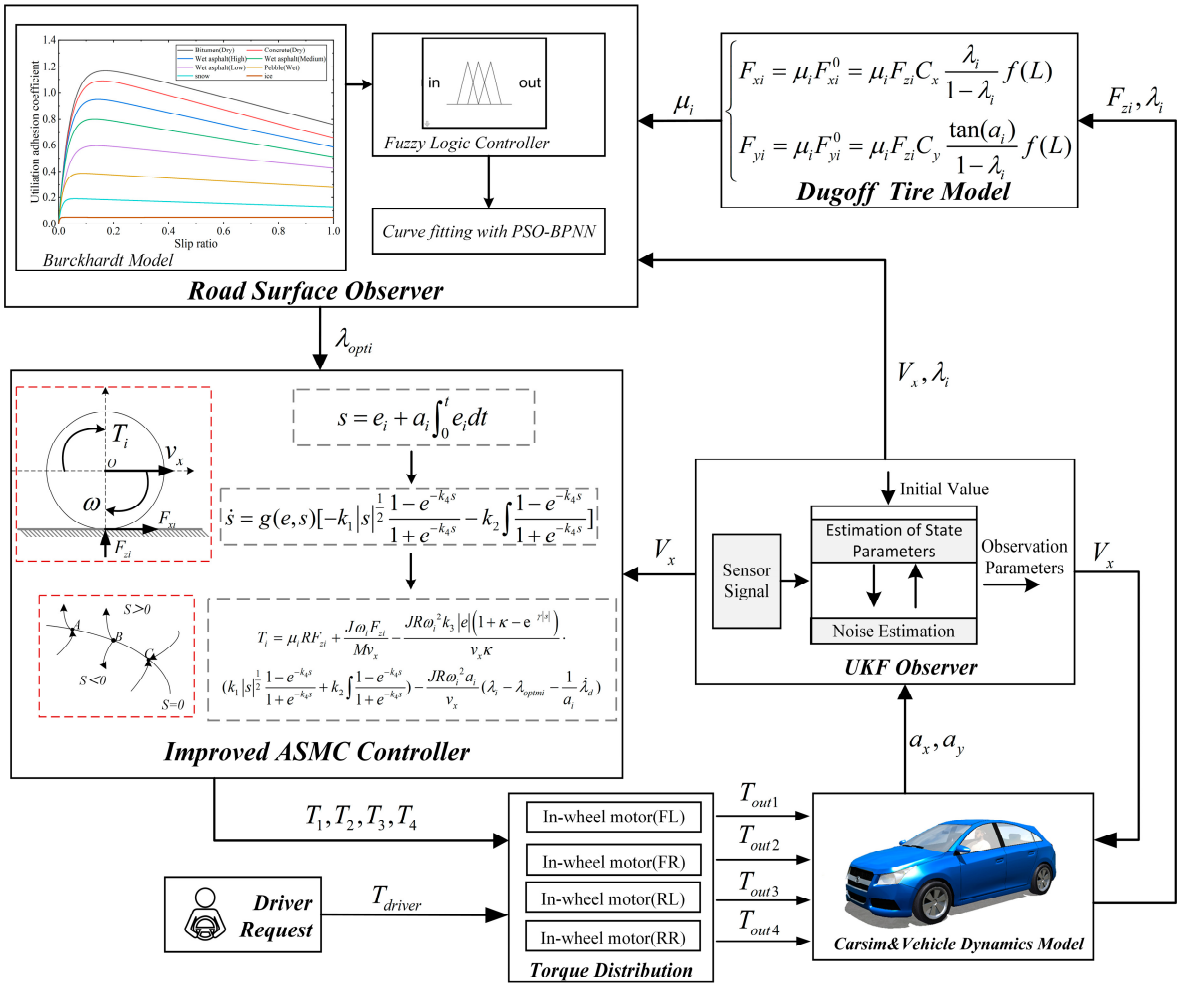

Figure 3. Architecture of the control system.

3.1. Longitudinal Vehicle Speed Estimator

3.1.1. UKF with Noise Estimation

In an anti-slip regulation system, longitudinal vehicle speed is key to calculating the current wheel slip ratio. Based on the modeling approach outlined in Section 2, this section adopts the 7DOF vehicle model, simplified to a 3DOF model for more direct and efficient longitudinal speed estimation, as shown in Figure 4. On this basis, the vehicle speed is estimated using the Unscented Kalman Filter (UKF). To address the real-time variations in system noise, the traditional UKF has been improved by incorporating real-time noise estimation, which enhances the accuracy of the speed estimation.

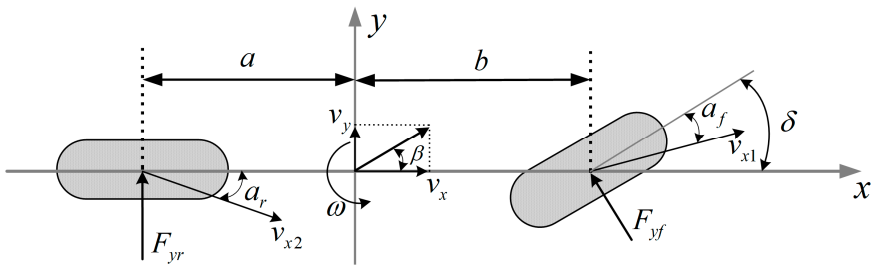

Figure 4. DOF vehicle dynamics model.

Assume a nonlinear system as shown below:

$$\begin{cases} x_{k+1} = f(x_k, u_k, w_k) \\ z_k = h(x_k, v_k) \end{cases} \tag{21}$$

where f is the nonlinear state equation, h is the nonlinear observation equation, w is the process noise with a covariance of Q, and v represents the observation noise with a covariance of R.

The core of the UKF method is the Unscented Transform (UT). For a nonlinear system $y = f(x)$, the mean of $y = f(x)$ is donated as $\overline{x}$ and variance is P. Thus, the Unscented Transform (UT) can be used to generate $2n + 1$ sampling points (i.e., Sigma points) χ and their corresponding weights ω to estimate the statistical parameters of $y = f(x)$.

The steps of the Unscented Kalman Filter (UKF) are as follows.

Step 1: Determine $2n + 1$ Sigma points, where n is the dimension of the state.

$$\begin{cases} \chi_{(0)} = \overline{x}, i = 0 \\ \chi_{(i)} = \overline{x} + (\sqrt{(n+\lambda)P})_i, i = 1, 2, \ldots, n \\ \chi_{(i)} = \overline{x} - (\sqrt{(n+\lambda)P})_i, i = n+1, n+2, \ldots, 2n \end{cases} \tag{22}$$

where $\left(\sqrt{P}\right)^T\left(\sqrt{P}\right) = P, \left(\sqrt{P}\right)_i$ represents the ith column of the square root of the covariance matrix P.

Step 2: Calculate the corresponding weights for these sampling points.

$$\begin{cases} \omega_{(0)}^m = \frac{\lambda}{n+\lambda} \\ \omega_{(0)}^c = \frac{\lambda}{n+\lambda} + (1 - a^2 + \beta) \\ \omega_{(i)}^m = \omega_c^{(i)} = \frac{1}{2(n+\lambda)}, i = 1, 2, \ldots, 2n \end{cases} \tag{23}$$

where m represents the corresponding weight for the mean, c (with a superscript) represents the corresponding weight for the covariance, c (with a subscript) indicates the number of sampling points; $\lambda = a^2(n + \kappa) - n$ is a scaling factor, which is used to reduce prediction errors; a controls the distribution of the sampling points; κ is a second-order scaling parameter, ensures that $(n + \lambda)P$ is a semi-positive definite matrix; and β is a weight coefficient.

Step 3: Obtain the set of Sigma points and the corresponding weights based on Equation (23):

$$\chi_{(i)k} = \left[\widehat{x}_k \quad \widehat{x}_k + \sqrt{(n+\lambda)P_k} \quad \widehat{x}_k - \sqrt{(n+\lambda)P_k}\right] \tag{24}$$

Step 4: The further prediction of the $2n + 1$ Sigma is:

$$\chi_{(i)k+1}^- = f\left(\chi_{(i)k}\right) \tag{25}$$

Step 5: The system state prediction and covariance matrix is:

$$\widehat{x}_{k+1}^- = \sum_{i=0}^{2n} \omega_{(i)}^m \chi_{(i)k+1}^- \tag{26}$$

$$P_{k+1}^- = \sum_{i=0}^{2n} \omega_{(i)}^0 \left[\widehat{x}_{k+1}^- - \chi_{(i)k+1}^-\right]\left[\widehat{x}_{k+1}^- - \chi_{(i)k+1}^-\right]^T + Q \tag{27}$$

Step 6: Generate the predicted sampling points through the Unscented Transform from the state predictions calculated in the previous step:

$$\chi_{(i)k+1}^- = \left[\widehat{x}_{(i)k+1}^- \quad \widehat{x}_{k+1}^- + \sqrt{(n+\lambda)P_{k+1}^-} \quad \widehat{x}_{k+1}^- - \sqrt{(n+\lambda)P_{k+1}^-}\right] \tag{28}$$

Step 7: The observations of the Sigma points are:

$$z^{-}_{(t)k+1} = h(\chi^{-}_{(t)k+1}) \tag{29}$$

Step 8: Obtain the predicted mean of the observations and the system's predicted mean and covariance through a weighted sum.

$$z^{-}_{k+1} = \sum_{t=0}^{2n} \omega^{m}_{(i)} Z^{-}_{(i)k+1} \tag{30}$$

$$P_{zz} = \sum_{i=0}^{2n} \omega^{c}_{(i)} \left[\widehat{z}^{-}_{k+1} - Z^{-}_{(i)k+1}\right] \left[\widehat{z}^{-}_{k+1} - Z^{-}_{(i)k+1}\right]^{T} + R_k \tag{31}$$

$$P_{xz} = \sum_{i=0}^{2n} \omega^{c}_{(i)} \left[\widehat{z}^{-}_{k+1} - \chi^{-}_{(i)k+1}\right] \left[\widehat{z}^{-}_{k+1} - Z^{-}_{(i)k+1}\right]^{T} \tag{32}$$

Step 9: The Kalman gain is:

$$K_{k+1} = P_{xz} P^{-1}_{zz} \tag{33}$$

Step 10: The system and state update, as well as the covariance update, are as follows:

$$\widehat{x}_{k+1} = \widehat{x}_{k+1} + K_{k+1}\left(z_{k+1} - \widehat{z}_{k+1}\right) \tag{34}$$

$$P_{k+1} = P^{-}_{k+1} + K_{k+1} P_{zz} K^{T}_{k+1} \tag{35}$$

Step 11: The noise estimation is:

$$\widehat{r}_{k+1} = (1 - d_k)\widehat{r}_k + d_k(z_{k+1} - \widehat{z}_{k+1}) \tag{36}$$

$$\varepsilon_{k+1} = z_{k+1} - \widehat{z}^{-}_{k+1} - \widehat{r}_{k+1} \tag{37}$$

$$\widehat{R}_{k+1} = (1 - d_k)\widehat{R}_k + d_k\left(\varepsilon_{k+1}\varepsilon^{T}_{k+1} - P_{zz}\right) \tag{38}$$

$$d_k = \frac{1 - c}{1 - c^{k+1}} \tag{39}$$

In Equation (39), c represents the forgetting factor, which measures the rate at which old data is forgotten.

3.1.2. Design of UKF Observer

Using the UKF algorithm to build the observer, according to d'Alembert's principle, the dynamic equilibrium equations for the vehicle body in the lateral, longitudinal, and yaw directions are as follows:

$$\sum F_x = ma_x \tag{40}$$

$$\sum F_y = ma_y \tag{41}$$

$$\sum M_z = I_z \dot{\gamma} \tag{42}$$

Substitute the vehicle state parameters:

$$-F_{yf} \sin\delta = ma_x \tag{43}$$

$$F_{yf} \cos\delta + F_{yr} = ma_y \tag{44}$$

$$aF_{yf}\cos\delta - bF_{yr} = I_z\dot{\omega} \tag{45}$$

The components of the absolute acceleration at the center of mass in the x and y directions within the xoy plane are:

$$a_x = \dot{v}_x - \dot{v}_y\gamma \tag{46}$$

$$a_y = \dot{v}_y + \dot{v}_x\gamma \tag{47}$$

Research shows that when the tire slip angle is controlled at 5°, the lateral force and slip angle of the tire have an approximately linear relationship. The simple linear tire model can be written in the following form (where k represents the tire's cornering stiffness).

$$F_{yf} = k_f a_f \tag{48}$$

$$F_{yr} = k_r a_r \tag{49}$$

By analyzing Figure 4, the expressions for calculating the front and rear wheel slip angles, as well as the slip angle at the center of mass of the vehicle, are as follows:

$$a_f = \beta + \frac{a\gamma}{v_x} - \delta \tag{50}$$

$$a_r = \beta - \frac{b\gamma}{v_x} \tag{51}$$

$$\beta = \frac{v_y}{v_x} \tag{52}$$

Substituting Equations (46)–(52) into (43)–(45) and simplifying, the following state equations and measurement equations are obtained:

$$\begin{cases} \dot{\gamma} = \frac{\left(a^2k_f + b^2k_r\right)}{I_z v_x}\gamma + \frac{\left(ak_f - bk_r\right)}{I_z}\beta - \frac{ak_f}{I_z}\delta \\ \dot{\beta} = \left(\frac{ak_f - bk_r}{mv_x{}^2} - 1\right)\gamma + \frac{k_f + k_r}{mv_x}\beta - \frac{k_f}{mv_x}\delta \\ \dot{v}_x = \gamma\beta v_x + a_x \end{cases} \tag{53}$$

$$a_y = \frac{ak_f - bk_r}{mv_x}\gamma + \frac{k_f + k_r}{m}\beta - \frac{k_f}{m}\delta \tag{54}$$

Rewriting the dynamic equations of Equations (53) and (54) into state-space form, the state equation and observation equation based on the three-degree-of-freedom nonlinear vehicle model are as follows:

$$\begin{cases} \dot{x}(t) = f(x(t), u(t), w(t)) \\ y(t) = h(x(t), v(t)) \end{cases} \tag{55}$$

where $x(t) = [\gamma \quad \beta \quad v_x]^T$ are the state variables, $u(t) = [\delta \quad a_x]^T$ are the input variables, a_y are the observation variables, and $x(t), v(t)$ are the system noise and measurement noise, respectively, both with a mean of zero. In summary, the schematic diagram of the improved UKF observer used for parameter estimation in this paper is shown in Figure 5:

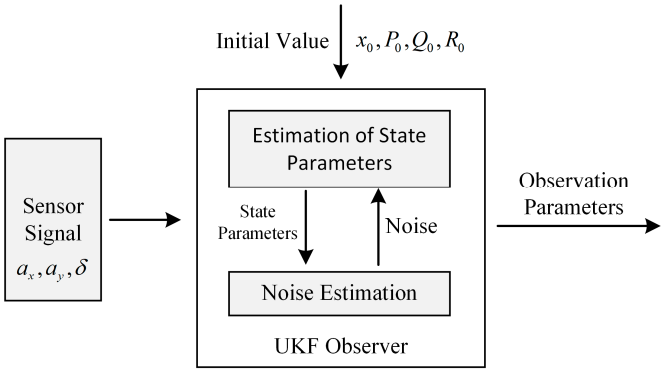

Figure 5. Structure of the UKF observer.

3.2. Design of Road Surface Observer

3.2.1. Design Process

The maximum road adhesion coefficient determines anti-slip regulation efficiency, while the optimal wheel slip ratio affects how well the vehicle uses road grip. The main goal of anti-slip regulation is to maximize road adhesion. Therefore, identifying the current road surface is essential. Figure 6 shows the process of observing longitudinal vehicle speed and road surface.

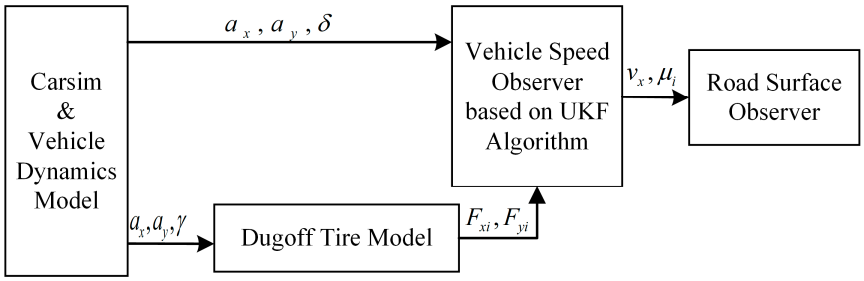

Figure 6. Road surface observer parameter acquisition.

First, the slip ratio is calculated using the wheel speed and vehicle speed from Carsim. The actual slip ratios of the four driving wheels are then input into the road surface observer. Next, the road adhesion coefficient is calculated and sent to the observer. The fuzzy road surface observer uses these inputs and applies fuzzy logic based on the Burckhardt tire model to estimate the similarity to standard road surfaces. Finally, the maximum road adhesion and optimal slip ratio for the current surface are determined.

3.2.2. Standard $\lambda-\mu$ Curve Acquisition

The establishment of fuzzy rules requires inputting the maximum available adhesion coefficient and the corresponding optimal slip ratio for different standard road surfaces. The most representative is the $\lambda - \mu$ function curve proposed by Burckhardt et al. [31], which shows the trend between the road adhesion coefficient and the slip ratio for different standard road surfaces through a fitted function. The fitting function is as follows:

$$\mu(\lambda) = C_1(1 - e^{-C_2\lambda}) - C_3\lambda \tag{56}$$

where C_1, C_2, C_3 are the fitting coefficients.

Selected 8 types of classic road surfaces and their related parameters are shown in Table 1:

Table 1. Fitting parameters for different road Surfaces.

Road Type	C_1	C_2	C_3	λ_{opt}	$\mu_{\max}$
Bitumen (Dry)	1.281	23.993	0.520	0.170	1.171
Concrete (Dry)	1.196	25.166	0.539	0.160	1.092
Wet asphalt (High)	1.027	29.494	0.442	0.143	0.950
Wet asphalt (Medium)	0.856	33.281	0.345	0.131	0.800
Wet asphalt (Low)	0.628	33.768	0.200	0.110	0.600
Pebble (Wet)	0.400	60.010	0.120	0.088	0.386
snow	0.195	94.129	0.065	0.065	0.190
ice	0.050	306.390	0.001	0.030	0.050

From Equation (56), the maximum available adhesion coefficient of the wheel and the corresponding optimal slip ratio can be derived. The equation is as follows:

$$\lambda_{opt} = \frac{1}{C_2} \ln \frac{C_1 C_2}{C_3} \tag{57}$$

$$\mu_{\max} = C_1 + \frac{C_3}{C_2}(1 - \ln \frac{C_1 C_2}{C_3}) \tag{58}$$

where λ_{opt} is the optimal slip ratio of the wheel under standard road surfaces, and $\mu_{\max}$ is the maximum available adhesion coefficient of the wheel under standard road surfaces. The resulting standard curve is shown in Figure 7.

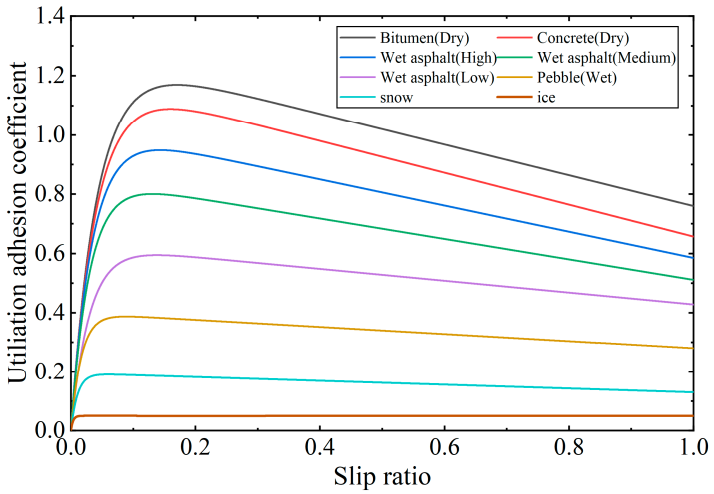

Figure 7. Relationship between slip ratio and adhesion coefficient for different road surfaces.

3.2.3. Design of Road Surfaces Observer Based on Fuzzy Control

To identify the road surface, the first step is to obtain the slip ratio and adhesion coefficient for each wheel [32], the details are as follows:

$$\lambda_i = \frac{\omega_i R - v_x}{\omega_i R} \tag{59}$$

$$\mu_i = \frac{F_{xi}}{F_{zi}} \tag{60}$$

The slip ratio is fuzzified into three subsets: large, medium, and small. Based on different slip ratio conditions, the adhesion coefficient is also fuzzified. Given the high accuracy and moderate computational complexity of the triangular membership function, it is primarily used for fuzzification. Based on the $\lambda - \mu$ curves for standard road surfaces, the relationship between the wheel adhesion coefficient and slip ratio varies. When the slip ratio is below 0.03, the differences between the curves are minimal, and overlap occurs,

making road surface identification difficult. Therefore, this range is fuzzified as a straight line, assuming a dry asphalt surface, and classified as a low slip ratio subset. For slip ratios between 0.03 and 0.15, road adhesion remains low, and the differences between surfaces are small, leading to the fuzzification of this range as a medium slip ratio subset. When the slip ratio exceeds 0.15 but remains below 0.2, the adhesion coefficient reaches its peak, with significant differences between road surfaces, allowing accurate identification. For slip ratios greater than 0.2, although adhesion starts to decline, the system can still distinguish between surfaces, so this range is classified as a high slip ratio subset. The membership functions are depicted in Figure 8.

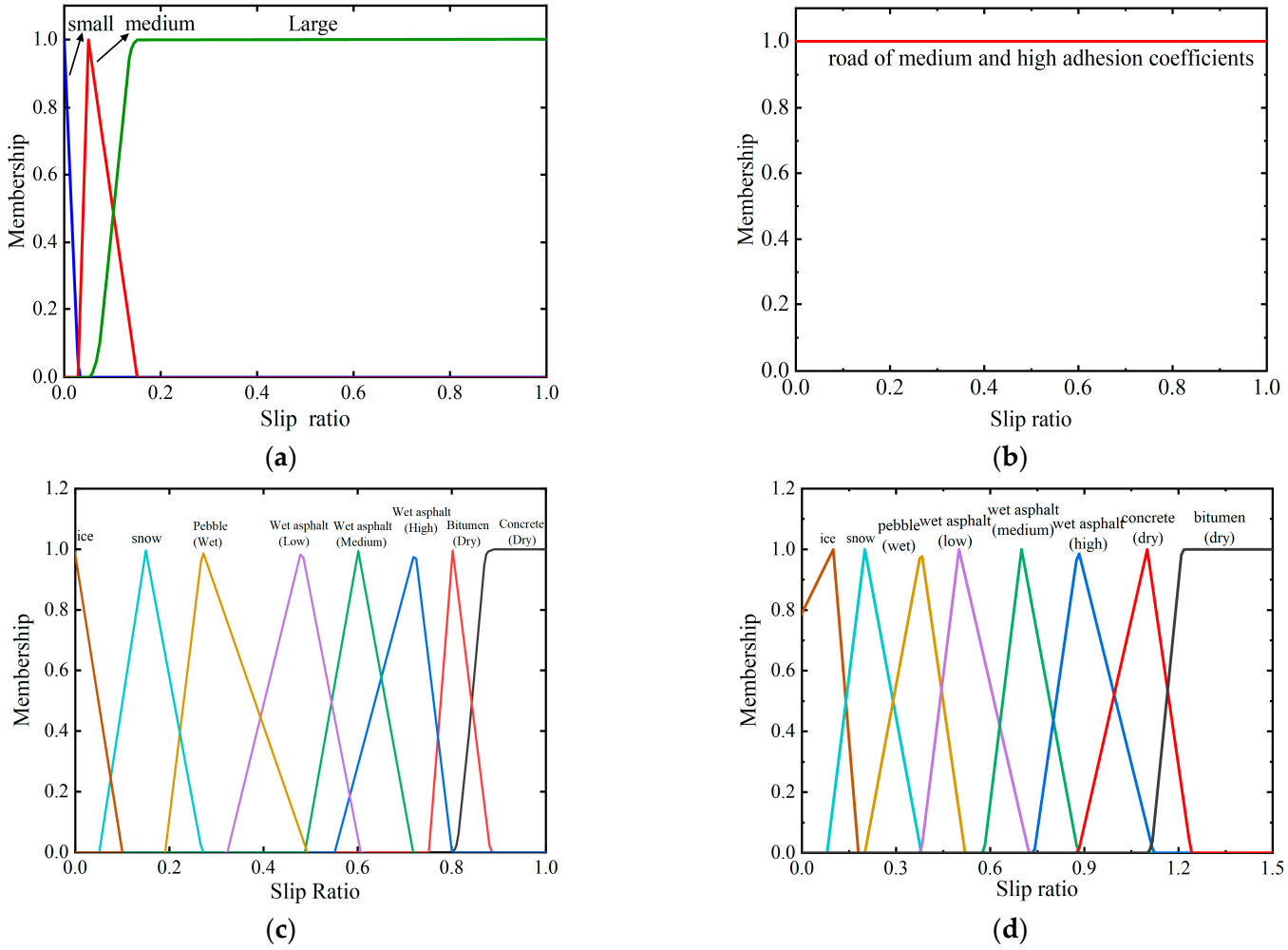

Figure 8. Design of membership function: (**a**) Slip ratio membership function; (**b**) Small slip ratio membership function; (**c**) Medium slip ratio membership function; (**d**) Large slip ratio membership function.

Finally, Table 2 presents 17 fuzzy rules for the road observer based on the fuzzy algorithm. The fuzzy universe is [HD, GD, M, GS, HS], and the output variable represents the fuzzy states of similarity to eight typical road surfaces, including high similarity (HS), general similarity (GS), moderate similarity (M), general dissimilarity (GD), and high dissimilarity (HD). Ultimately, the area centroid method is used to resolve the fuzziness.

Table 2. Fuzzy rule table.

Input		Output							
Slip Ratio	**Utilization Adhesion Coefficient**	**RH**	**RG**	**RF**	**RE**	**RD**	**RC**	**RB**	**RA**
Large	RA	HD	HD	HD	HD	HD	HD	GD	HS
Large	RB	HD	HD	HD	HD	HD	GD	HS	M
Large	RC	HD	HD	HD	GD	M	HS	GS	GD
Large	RD	HD	GD	M	GS	HS	M	HD	HD
Large	RE	GD	M	GS	HS	GS	GD	HD	HD
Large	RF	GD	GS	HS	GS	M	HD	HD	HD
Large	RG	GS	HS	GS	M	M	GD	HD	HD
Large	RH	HS	GS	M	M	M	GD	HD	HD
Medium	RA	HD	HD	HD	HD	HD	HD	GD	HS
Medium	RB	HD	HD	HD	HD	HD	GD	HS	M
Medium	RC	HD	HD	HD	GD	GS	HS	GS	GD
Medium	RD	HD	HD	GS	GS	HS	M	HD	HD
Medium	RE	M	M	GS	HS	GS	GD	HD	HD
Medium	RF	GS	GS	HS	GS	M	HD	HD	HD
Medium	RG	HS	HS	GS	GS	M	GD	HD	HD
Medium	RH	HS	HS	GS	GS	M	GD	HD	HD
Small	RI	HS	HS	HS	HS	HD	HD	HD	HD

The similarity coefficient output by the fuzzy inference is a fuzzy value, which needs to be defuzzified to obtain a precise numerical value. This paper uses the weighted average method for defuzzification, which has low computational complexity and good continuity. To optimize the weight distribution, the Gaussian membership function, known for its high discriminative power, is selected. The similarity membership function is shown in Figure 9.

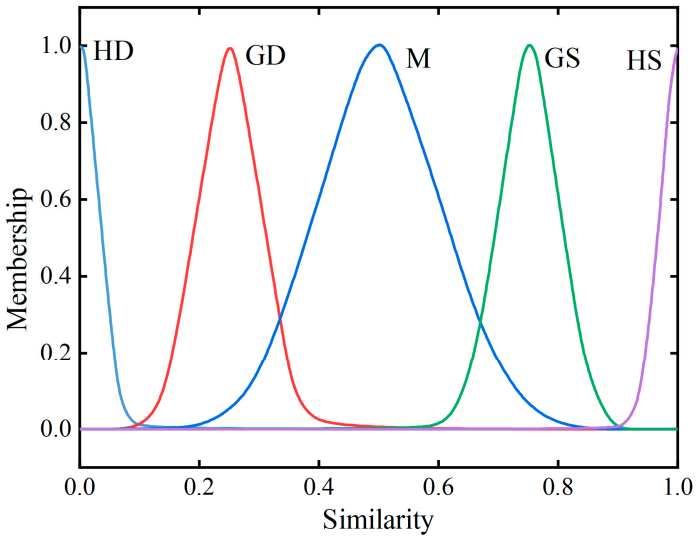

Figure 9. Similarity membership function.

Based on the precise similarity coefficient obtained after defuzzification, the current road surface's maximum available adhesion coefficient $\mu_{\max}$ and the corresponding optimal slip ratio λ_{opt} can be determined. The calculation formula is as follows:

$$\mu_{\max} = \frac{\sum_{\sigma=1}^{8} x_\sigma \mu_{\max\sigma}}{\sum_{\sigma=1}^{8} x_\sigma} \tag{61}$$

$$\lambda_{opt} = \frac{\sum_{\sigma=1}^{8} x_\sigma \lambda_{opt\sigma}}{\sum_{\sigma=1}^{8} x_\sigma} \tag{62}$$

where x_σ is the similarity coefficient between the driving road and each typical road surface $\sigma = 1, 2, \ldots, 8$.

By calculating the maximum adhesion coefficient of the current road surface and estimating the optimal slip ratio based on the maximum adhesion coefficient-optimal slip ratio curve, a data fitting method was employed to establish the mathematical relationship between the maximum adhesion coefficient and the optimal slip ratio for typical road surfaces. Given that the BP neural network has excellent nonlinear mapping capabilities, it can accurately approximate any continuous nonlinear function [33]. Therefore, the BP neural network algorithm is used for the fitting operation in this paper. The schematic diagram of the BP neural network is shown in Figure 10.

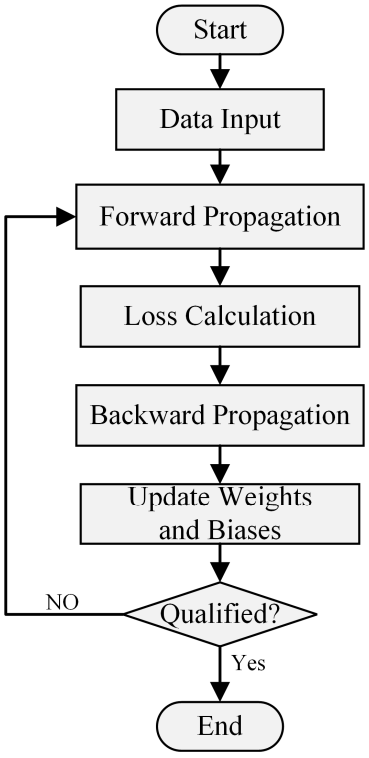

Figure 10. BP neural network framework.

This paper uses the PSO algorithm to optimize the BP neural network. PSO enhances the global search capability of the BP neural network, prevents local optima, and accelerates convergence by finding better initial weights and biases. The PSO–BP neural network shows excellent performance in data fitting. As shown in Figure 11, the fitted maximum adhesion coefficient-optimal slip ratio curve closely matches the data points, effectively representing their relationship.

In this section, the target optimal slip ratio of the wheel under the current operating conditions is determined by combining the road observer with fuzzy control and the PSO-optimized BP neural network.

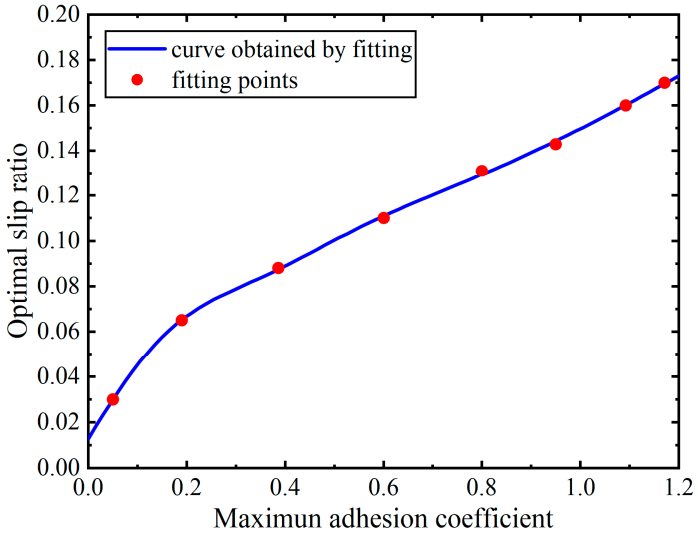

Figure 11. Fitted curve for $\lambda_{optimal} - \mu_{\max}$.

3.3. Design of the Anti-Slip Regulation Controller Based on Optimal Slip Ratio

The design process of the improved ASMC controller proposed in this paper is shown in Figure 12:

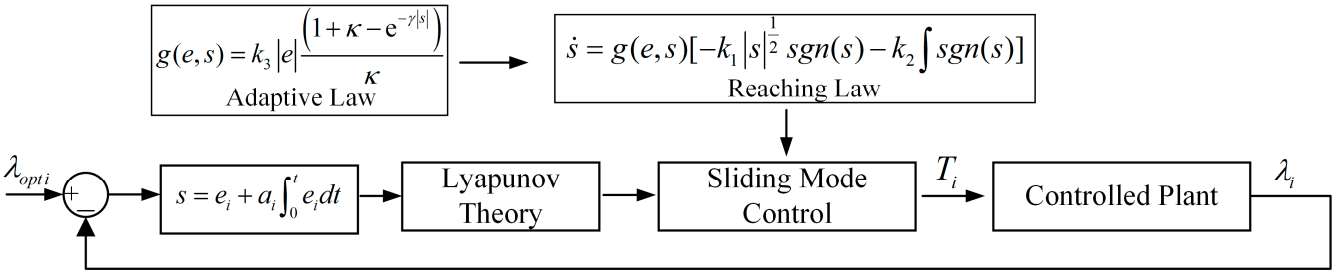

Figure 12. Design process of improved ASMC controller design process.

After obtaining the optimal slip ratio, the actual slip ratio of each drive wheel needs to be adjusted to approach this value, thus achieving ASR control. In this paper, an anti-slip driving controller based on an optimized adaptive sliding mode algorithm is constructed. To enhance control performance, the sliding mode surface and reaching law are optimized, and the adaptive law is improved to enhance robustness. This controller adjusts the output torque according to the target slip ratio, ensuring that the wheel slip ratio approaches the optimal level. Based on the slip ratio formula and the single-wheel dynamics model, an improved adaptive sliding mode controller is designed. When the system approaches the sliding mode surface, the system inertia is reduced by lowering the approaching speed, effectively weakening the chattering phenomenon.

$$\dot{\lambda}_i = \frac{\dot{\omega}_i v_x - \omega_i \dot{v}_x}{R\omega_i{}^2} \tag{63}$$

Substituting Equations (9)–(11) into Equation (63) yields:

$$\dot{\lambda}_i = \frac{v_x T_i}{JR\omega_i{}^2} - \mu_i\left(\frac{F_{zi}v_x}{J\omega_i{}^2} + \frac{F_{zi}}{RM\omega_i}\right) \tag{64}$$

In the equation, some parameters are obtained through parameter estimation, v_x is obtained by the UKF observer, and F_{zi} is calculated based on the vertical loads of each

wheel as described earlier. The error between the actual slip ratio and the desired slip ratio for each wheel can be expressed as:

$$e_i = \lambda_i - \lambda_{opti} \tag{65}$$

To better eliminate the steady-state error in slip ratio control, a proportional–integral sliding mode surface is designed:

$$s = e_i + a_i \int_0^t e_i dt \tag{66}$$

where a_i is the gain parameter.

In the sliding mode control process, selecting an appropriate reaching law can ensure the reaching speed during the reaching phase while improving the dynamic performance of the system in the sliding mode phase. To satisfy the reaching conditions of sliding mode control and balance both reaching speed and reaching quality, this paper first introduces the concept of super-twisting sliding mode control and uses a nonlinear reaching law, which is specifically expressed as:

$$\dot{s} = -k_1 |s|^{\frac{1}{2}} sgn(s) - k_2 \int sgn(s) \tag{67}$$

where k_1 and k_2 are the control gain parameters. By introducing the concept of the super-twisting algorithm, its robustness can be improved to a certain extent.

Furthermore, to make the controller adaptable to complex systems and capable of automatically adjusting control parameters, the concept of adaptive control is introduced, and an adaptive rate $g(e, s)$ is designed. The design principle is that during the reaching phase of the sliding surface, the adaptive rate $g(e, s)$ should be relatively large to allow the system to quickly enter the sliding mode. In the sliding mode state, $g(e, s)$ should be set small enough to reduce chattering.

Based on the above principles, the adaptive rate $g(e, s)$ is designed for the sliding surface.

$$g(e, s) = k_3 |e| \frac{\left(1 + \kappa - \mathrm{e}^{-\gamma |s|}\right)}{\kappa} \geq 0 \tag{68}$$

where $0 < \kappa < 1$, $\gamma > 0$, and $\lim_{t \to \infty} |e| = 0$.

By adding the adaptive law Equation (67) to Equation (68), the following equation is obtained:

$$\dot{s} = g(e, s)[-k_1 |s|^{\frac{1}{2}} sgn(s) - k_2 \int sgn(s)] \tag{69}$$

$$\dot{s} = k_3 |e| \frac{\left(1 + \kappa - \mathrm{e}^{-\gamma |s|}\right)}{\kappa} [-k_1 |s|^{\frac{1}{2}} sgn(s) - k_2 \int sgn(s)] \tag{70}$$

In the equation, the controller uses the sign function $sgn(s)$, which is a discontinuous function. This discontinuity can adversely affect the control system by introducing chattering. To mitigate the chattering in the control system, the following continuous function $f(x)$ is used to replace the sign function. The function $f(x)$ is given as:

$$f(x) = \frac{1 - e^{-k_4 s}}{1 + e^{-k_4 s}} \tag{71}$$

$$\dot{s} = k_3 |e| \frac{\left(1 + \kappa - \mathrm{e}^{-\gamma |s|}\right)}{\kappa} [-k_1 |s|^{\frac{1}{2}} sgn(s) - k_2 \int sgn(s)] \tag{72}$$

where k_4 is the parameter of the continuous function that is adjusted. The final adjusted reaching law is given as:

$$\dot{s} = k_3|e|\frac{\left(1+\kappa-\mathrm{e}^{-\gamma|s|}\right)}{\kappa}[-k_1|s|\frac{1}{2}\frac{1-e^{-k_4 s}}{1+e^{-k_4 s}} - k_2\int\frac{1-e^{-k_4 s}}{1+e^{-k_4 s}}] \tag{73}$$

Thus, the reaching law satisfies the existence condition of the generalized sliding mode and therefore meets both the existence and reachability conditions of the sliding mode. Substituting (66) into (73) yields:

$$\dot{s} = \dot{\lambda}_i - \dot{\lambda}_{opti} + a_i(\lambda_i - \lambda_{opti}) = k_3|e|\frac{\left(1+\kappa-\mathrm{e}^{-\gamma|s|}\right)}{\kappa}[-k_1|s|\frac{1}{2}\frac{1-e^{-k_4 s}}{1+e^{-k_4 s}} - k_2\int\frac{1-e^{-k_4 s}}{1+e^{-k_4 s}}] \tag{74}$$

After simplification, the following is obtained:

$$T_i = \mu_i R F_{zi} + \frac{J\omega_i F_{zi}}{M v_x} - \frac{JR{\omega_i}^2 k_3|e|\left(1+\kappa-\mathrm{e}^{-\gamma|s|}\right)}{v_x\kappa}\cdot(k_1|s|\frac{1}{2}\frac{1-e^{-k_4 s}}{1+e^{-k_4 s}} + k_2\int\frac{1-e^{-k_4 s}}{1+e^{-k_4 s}}) - \frac{JR{\omega_i}^2 a_i}{v_x}(\lambda_i - \lambda_{opti} - \frac{1}{a_i}\dot{\lambda}_{opti}) \tag{75}$$

Equation (75) represents the torque output of each wheel by the improved adaptive sliding mode control driving controller. After torque distribution, the optimal torque output is achieved by integrating the driver's request with the ASR anti-slip driving controller, ensuring optimal slip ratio tracking for each wheel.

To verify the stability of the system, the *Lyapunov* theory is used to prove the system's stability. The *Lyapunov* function can be expressed as:

$$V = \frac{1}{2}s^2 \tag{76}$$

By differentiating Equation (76), the following result can be obtained:

$$\dot{V} = s\dot{s} = sk_3|e|\frac{\left(1+\kappa-\mathrm{e}^{-\gamma|s|}\right)}{\kappa}[-k_1|s|\frac{1}{2}\frac{1-e^{-k_4 s}}{1+e^{-k_4 s}} - k_2\int\frac{1-e^{-k_4 s}}{1+e^{-k_4 s}}] \tag{77}$$

where $k_1, k_2, k_3, k_4, \gamma$ are the positive numbers, the analysis leads to the conclusion that:

$$\begin{cases} \dot{V} \le 0, s \le 0 \\ \dot{V} < 0, s > 0 \end{cases} \tag{78}$$

From the equation, it can be seen that $\dot{V}$ is always negative, therefore the improved adaptive sliding mode anti-slip regulation controller proposed in this paper is asymptotically stable and meets the design requirements.

3.4. Torque Request for the In-Wheel Motors

After requesting torque from the driver model, it is coordinated with the control torque from the improved adaptive anti-slip controller, and the final torque for each wheel is sent to the motor controller during vehicle acceleration.

$$T_{reqi} = T_{driver} + T_i \tag{79}$$

where T_{reqi} is the result of the combined torques, T_i is the adjusted torque output by the ASR controller, and T_{driver} is the torque requested by the driver. The control torque for each hub motor is derived by combining the current control torque calculated by each ASR controller with the basic driver's requested torque. This ensures that each wheel achieves optimal slip ratio control when driving on different road surfaces.

4. Simulation and Data Analysis

This paper conducts co-simulation based on Matlab/Simulink R2021a and Carsim 2020, with the simulation structure diagram shown in Figure 13.

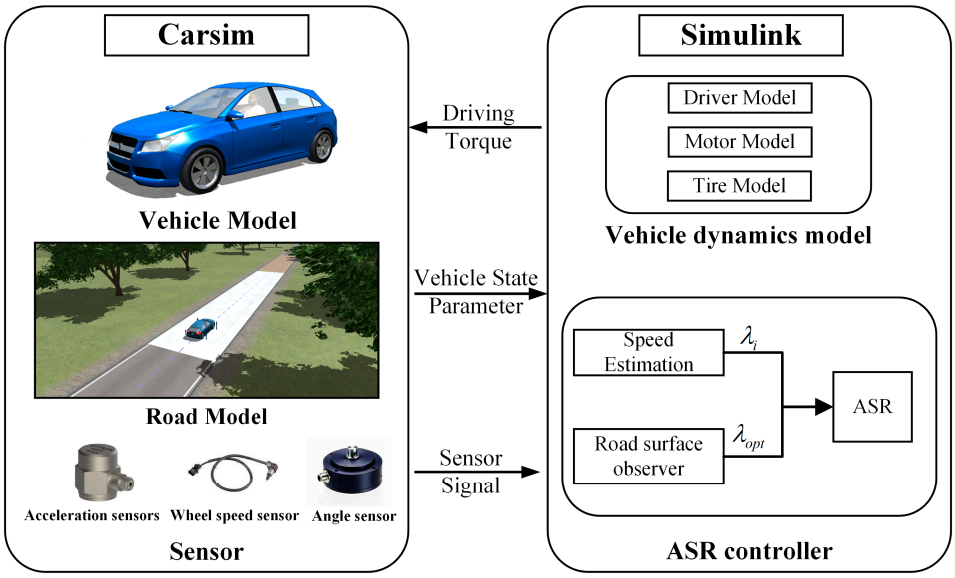

Figure 13. Simulation structure diagram.

To verify the drive anti-slip control strategy based on road surface recognition, this paper selects a low-adhesion surface (μ = 0.2), a straight road surface with three different adhesion coefficients (μ = 0.8, μ = 0.3, μ = 0.6), and a split road surface (μ = 0.8, μ = 0.3) for simulation. This analysis aims to verify the feasibility of the road surface observer and the accuracy of the improved adaptive anti-slip controller in tracking the optimal slip ratio. First, the vehicle model parameters established in Carsim are shown in Table 3.

Table 3. Vehicle parameters.

Parameters	Notation	Unit	Value
Vehicle mass	m	kg	1380
Distance from the center of mass to the front axle	A	m	1.26
Distance from the center of mass to the rear axle	B	m	1.38
Height of the center of mass	h_g	m	0.54
Effective radius of the tire	R_w	m	0.325
Vehicle moment of inertia around Z-axis	I_z	kg·m^2	1343.1
Tire moment of inertia	J_i	kg·m^2	1.5
Rated power of in-wheel motors	P	kw	70
Maximum speed of in-wheel motors	n	rpm	1500
Rated torque of in-wheel motors	T	Nm	500

4.1. Driving on a Low-Adhesion Road

The test road is set as a flat, straight road with an adhesion coefficient of 0.2, shown in Figure 14. The initial vehicle speed is set to 0 km/h, and the desired driver speed is set to 80 km/h.

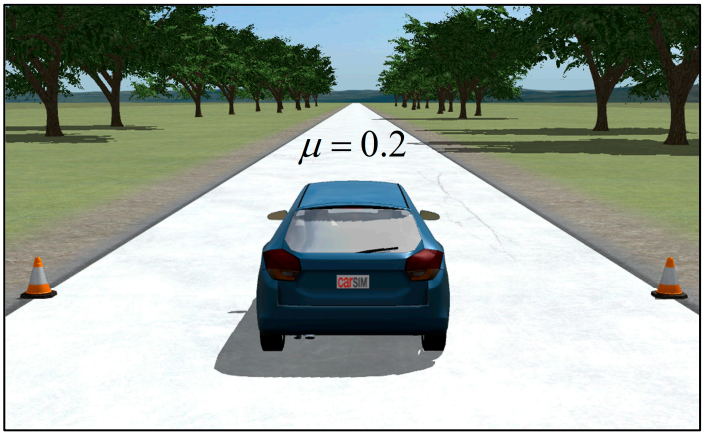

Figure 14. Simulation on a low-adhesion road.

The vehicle is accelerated on the set low-adhesion road surface, and the simulation results are shown in Figure 15.

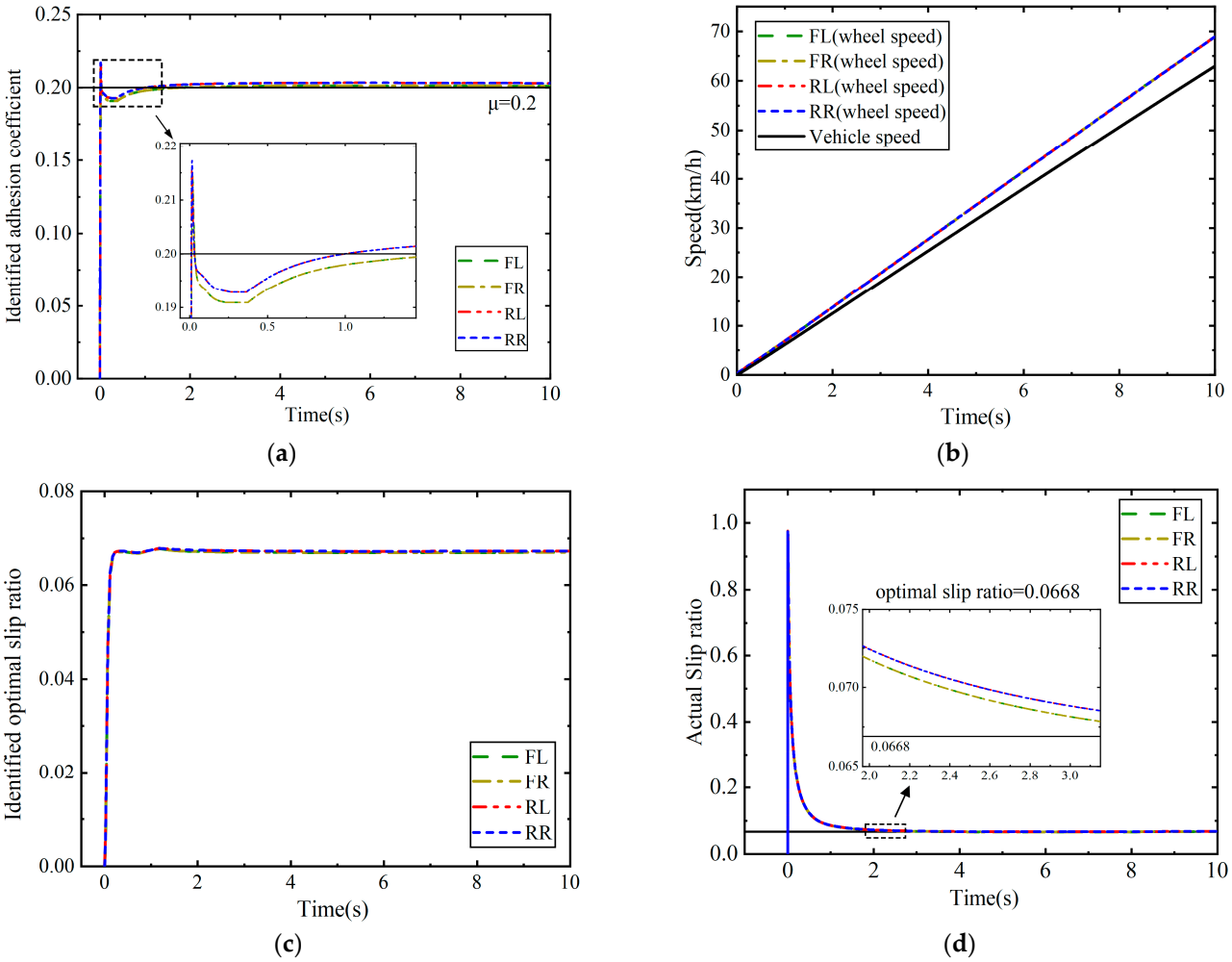

Figure 15. Simulation results of a low-adhesion road: (**a**) Identified adhesion coefficient; (**b**) Wheel speed; (**c**) Identified optimal slip ratio; (**d**) Actual slip ratio.

The simulation results show that as the vehicle begins to accelerate, both the wheel speeds and the vehicle speed increase. The road surface observer identifies the adhesion coefficients for the contact surfaces of each wheel. On the road with an adhesion coefficient

of 0.2, the identification results stabilize after approximately 2.3 s: 0.201 for the front wheels, with an error of 0.001, and 0.203 for the rear wheels, with an error of 0.003. This indicates that the road surface observer can effectively identify the adhesion coefficient under the low-adhesion road, thereby fitting the optimal target slip ratio.

At the moment the vehicle begins to accelerate, both the torque and slip ratio increase rapidly with vehicle speed. The initial slip ratio approaches 1 due to the vehicle and wheel speeds both being zero, causing a near-limit phenomenon when wheel speed is used as the denominator. After approximately 2.4 s, the slip ratios of all wheels gradually stabilize, with the front wheels' slip ratio remaining around 0.0665, with an error of 0.0003, and the rear wheels stabilizing at 0.067, with an error of 0.0002. Under ASR control, the tracking performance of the optimal slip ratio meets the required standards. The simulation results are summarized in Table 4.

Table 4. Results of the low-adhesion road.

Optimal Slip Ratio = 0.0668				
	FL-Wheel	FR-Wheel	RL-Wheel	RR-Wheel
Actual slip ratio	0.0665	0.0665	0.067	0.067
Absolute Error	0.0003	0.0003	0.0002	0.0002

To verify the effectiveness of the drive anti-slip control strategy in improving vehicle acceleration performance, a comparison of acceleration performance with and without the drive anti-slip function was conducted under the same simulation conditions. The simulation results are shown in Figure 16.

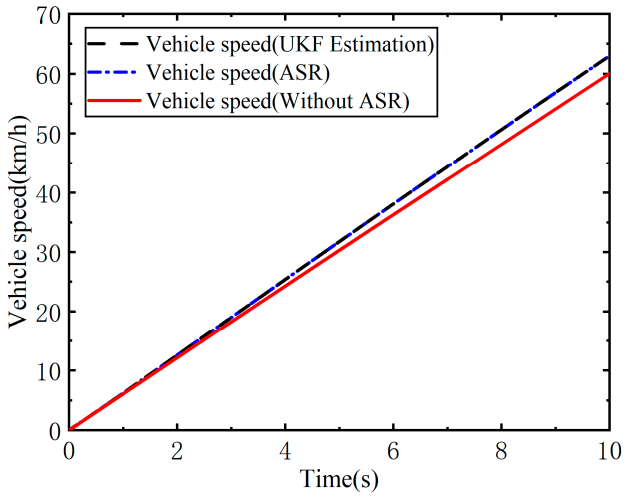

Figure 16. Comparison of longitudinal speed on low-adhesion road.

From the results, it can be seen that under the drive anti-slip controller used in this paper, the vehicle speed after 10 s of acceleration in the same conditions is 62.99 km/h, while without the drive anti-slip function, the speed at this point is 58.55 km/h. A comparison shows that on low-adhesion surfaces, the acceleration with drive anti-slip control is 1.7497, whereas without the drive anti-slip function, the acceleration is 1.63, representing an improvement of 0.119. Additionally, as shown in the figure, the UKF speed estimation can accurately estimate the longitudinal vehicle speed.

To verify the robustness of the drive anti-slip controller proposed in this paper, a comparison of simulation results with a conventional sliding mode controller is conducted (using the left front wheel as an example). Results are shown in Figure 17.

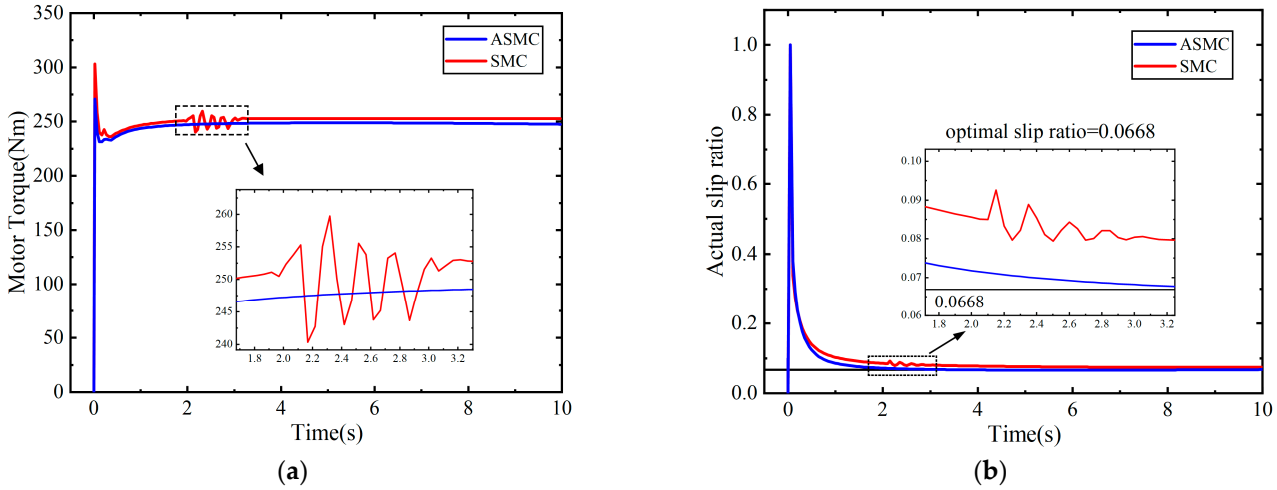

Figure 17. Comparison of different controllers on low-adhesion road: (**a**) Torque control comparison; (**b**) Actual slip ratio control comparison.

As shown in Figure 17a, the output torque under different control strategies increases instantly when acceleration starts at 0 s. The control torque gradually approaches a steady-state value within the 0–2 s interval, but the SMC control exhibits noticeable oscillations. This is because, when approaching the sliding mode surface, the control system experiences frequent switching near the surface, leading to high-frequency chattering. However, the improved ASMC proposed in this paper effectively mitigates the oscillation issue by using an adaptive law and adjusting the switching function.

As shown in Figure 17b, after the 2−s mark, there is some chattering in the slip ratio tracking, and the convergence time of the tracking slip ratio is relatively long. The tracking slip ratio for the conventional SMC is 0.0746, with an error of 0.0072, which indicates lower tracking accuracy compared to the improved ASMC. The comparison results are shown in Table 5.

Table 5. Comparison results of different algorithms of the low-adhesion road.

Optimal Slip Ratio = 0.0668		
	ASMC	SMC
Motor Torque (Nm)	248.5	252.9
Actual slip ratio	0.0665	0.0746
Absolute Error	0.0003	0.0072
Control accuracy	99.55%	89.22%

4.2. Driving on a Joint Road

The test road is set as a flat, joint road with step changes in adhesion coefficients (0.8–0.3–0.6), shown in Figure 18. The initial vehicle speed is set to 0 km/h, and the driver's desired speed is set to 80 km/h.

The vehicle is accelerated on the set joint road, and the simulation results are shown in Figure 19.

After the vehicle starts on the joint road surface, the wheel speeds gradually increase, and the road surface observer begins monitoring at 0.05 s. On the road surface with an adhesion coefficient of 0.8, the identified adhesion coefficient for the front axle wheels is 0.805, with an error of 0.005, and for the rear axle wheels, it is 0.803, with an error of 0.003. Compared to the ideal slip ratio of 0.1294, the actual slip ratio for the front axle is 0.1296, with an error of 0.0002, and for the rear axle, it is 0.1295, with an error of 0.0001. This indicates that the actual tracking performance meets expectations.

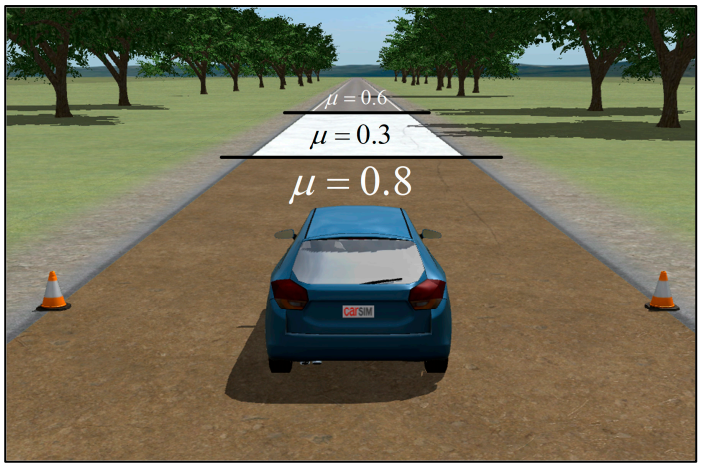

Figure 18. Simulation on a joint road.

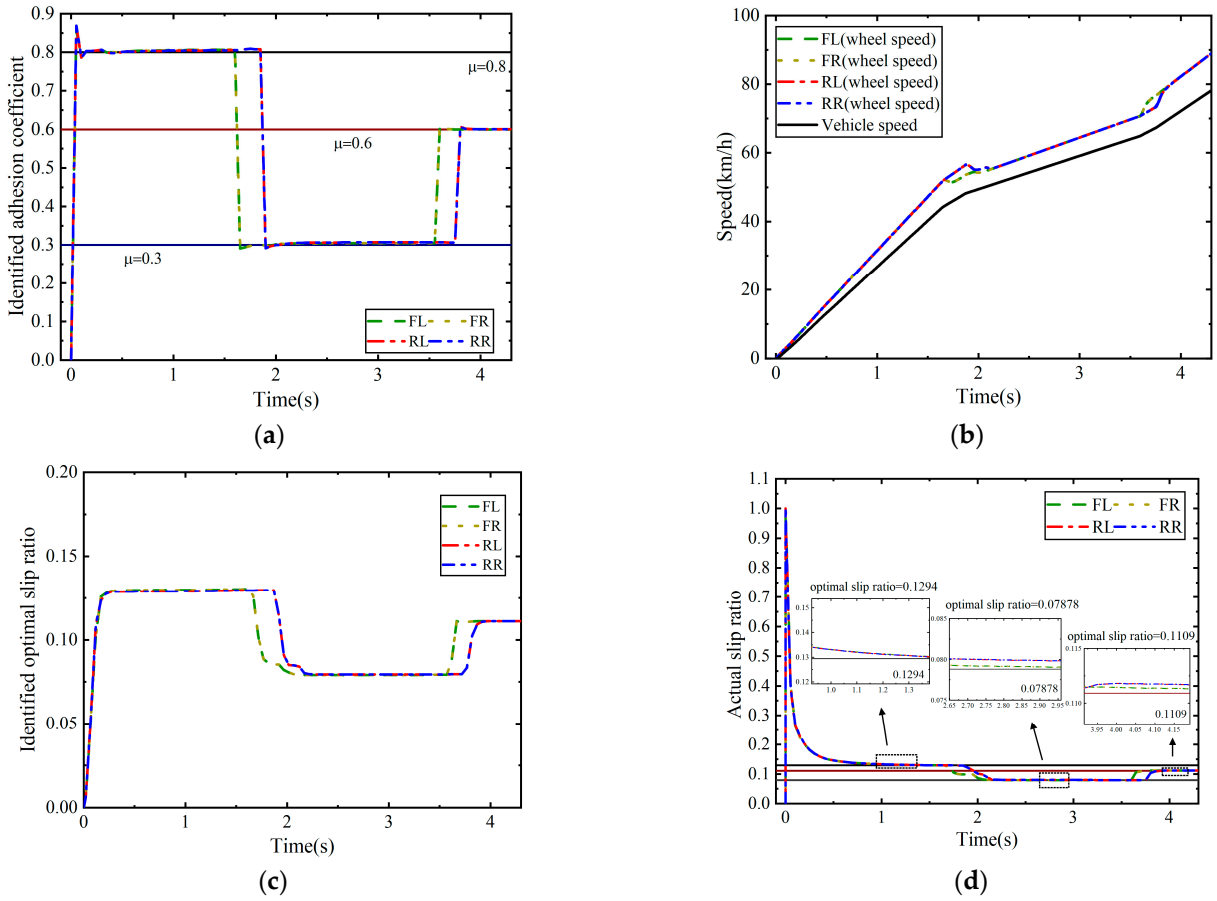

Figure 19. Simulation results of a joint road: (**a**) Identified adhesion coefficient; (**b**) Wheel speed; (**c**) Identified optimal slip ratio; (**d**) Actual slip ratio.

At 2 s, the front wheels first enter the low-adhesion road surface with an adhesion coefficient of 0.3, and the increase in wheel speed slows down to track the optimal slip ratio. Once the vehicle is fully on the low-adhesion surface, the identified adhesion coefficient for the front axle wheels is 0.304, with an error of 0.004, and for the rear axle wheels, it is 0.307, with an error of 0.007. Compared to the ideal slip ratio of 0.07878, the slip ratio for the front wheels is 0.0792, with an error of 0.00042, and for the rear wheels, it is 0.0797, with an error of 0.00092.

At 3.6 s, the front wheels enter the road surface with an adhesion coefficient of 0.6, and the increase in wheel speed accelerates to track the optimal slip ratio. Once the vehicle is fully on this surface, the identified adhesion coefficient for the front axle wheels is 0.6001, with an error of 0.0001, and for the rear axle wheels, it is 0.6004, with an error of 0.0004. Compared to the ideal slip ratio of 0.1109, the actual slip ratio for the front axle wheels is 0.11135, with an error of 0.00045, and for the rear axle wheels, it is 0.11174, with an error of 0.00084. This indicates that the control performance on this section of the road meets the expected results. The simulation results are summarized in Table 6.

Table 6. Results of the joint road.

Optimal Slip Ratio = 0.1294				
	FL-Wheel	FR-Wheel	RL-Wheel	RR-Wheel
Actual slip ratio	0.1296	0.1296	0.1295	0.1295
Absolute Error	0.0002	0.0002	0.0001	0.0001
Optimal Slip Ratio = 0.07878				
	FL-Wheel	FR-Wheel	RL-Wheel	RR-Wheel
Actual slip ratio	0.0792	0.0792	0.00797	0.0797
Absolute Error	0.00042	0.00042	0.00092	0.00092
Optimal Slip Ratio = 0.1109				
	FL-Wheel	FR-Wheel	RL-Wheel	RR-Wheel
Actual slip ratio	0.11135	0.11135	0.11174	0.11174
Absolute Error	0.00045	0.00045	0.00084	0.00084

To assess the impact of the drive anti-slip control strategy on acceleration performance, a comparison was made with and without the anti-slip function under the same conditions. The results are shown in Figure 20.

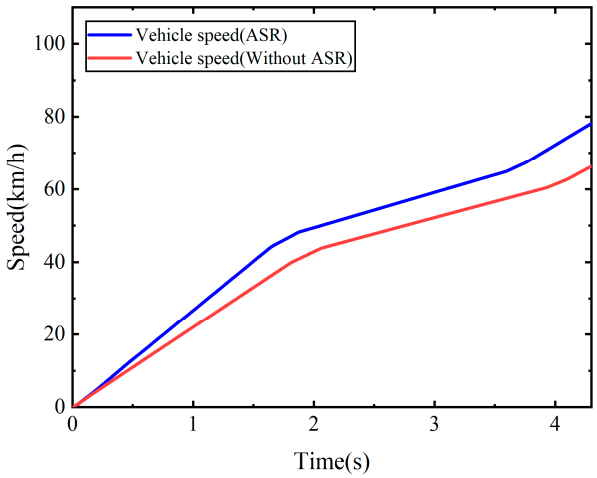

Figure 20. Comparison of longitudinal speed on a joint road.

The results show that with the drive anti-slip function enabled, the vehicle reached the target speed in 4.3 s, with a speed of 80.001 km/h, compared to 67.743 km/h without the function. The acceleration on the joint road surface was 5.05 m/s^2 with the anti-slip function, and 4.28 m/s^2 without it, an improvement of 0.77 m/s^2. This demonstrates that the drive anti-slip control significantly enhances vehicle acceleration performance.

To verify the robustness of the drive anti-slip controller proposed in this paper, a comparison of simulation results with a conventional sliding mode controller was conducted (using the left front wheel as an example). The results are shown in Figure 21.

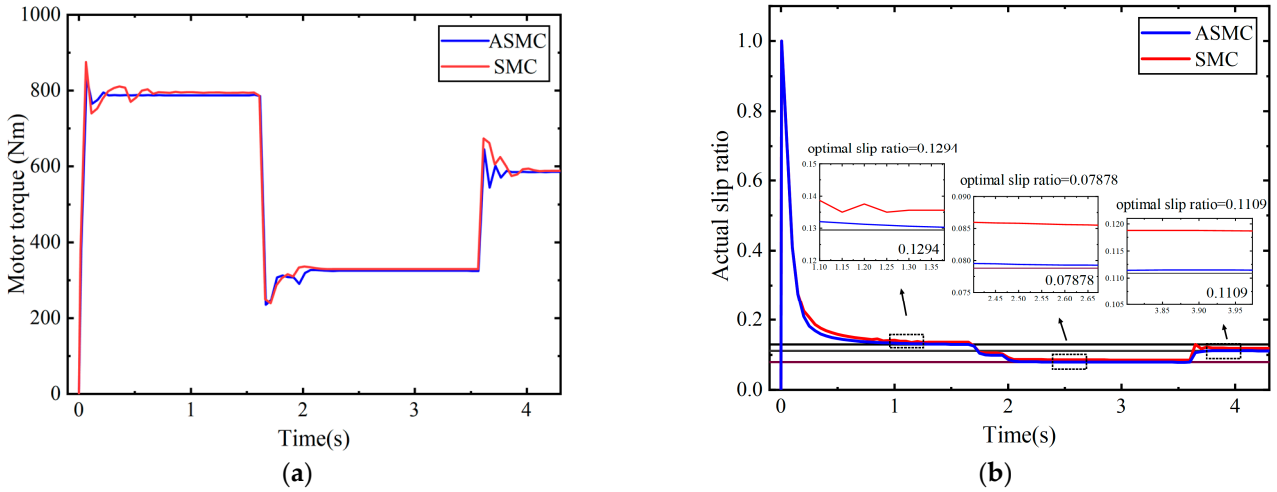

Figure 21. Comparison of different controllers on a joint road: (**a**) Torque control comparison; (**b**) Slip ratio control comparison.

As shown in Figure 21a, the output torque increases instantly at 0 s when acceleration begins. Between 0.2 and 0.5 s, the ASMC converges more quickly and reaches a steady state, while the SMC exhibits noticeable oscillations. Although the oscillation amplitude is small and its impact on the slip ratio is limited, the oscillation is still present. Based on road surface changes, the output torque quickly adjusts to control the slip ratio. However, under SMC control, there is a larger steady-state error and significant torque oscillation, which the ASMC effectively resolves.

As shown in Figure 21b, on a road surface with an adhesion coefficient of 0.8, the slip ratio under SMC control is 0.1356, with an error of 0.0062; on a 0.3 coefficient surface, the slip ratio is 0.0845, with an error of 0.0057; and on a 0.6 surface, the slip ratio is 0.1186, with an error of 0.0077. Compared to the improved ASMC, the control performance of SMC still shows a gap. The comparison results are shown in Table 7.

Table 7. Comparison results of different algorithms of the joint road.

Optimal Slip Ratio = 0.1294		
	ASMC	SMC
Motor torque (Nm)	787.6	795.1
Actual slip ratio	0.1296	0.1356
Absolute Error	0.0002	0.0062
Control accuracy	99.84%	95.2%
Optimal Slip Ratio = 0.07878		
	ASMC	SMC
Motor torque (Nm)	325.1	329.5
Actual slip ratio	0.0792	0.0845
Absolute Error	0.00042	0.0057
Control accuracy	99.47%	92.76%
Optimal Slip Ratio = 0.1109		
	ASMC	SMC
Motor torque (Nm)	585.5	588.7
Actual slip ratio	0.11135	0.1186
Absolute Error	0.00045	0.0077
Control accuracy	99.59%	93.5%

4.3. Driving on a Split Road

The test road is set as a straight split road (left side adhesion coefficient of 0.8, right side adhesion coefficient of 0.2), with an initial vehicle speed of 0 km/h and a desired driver speed of 80 km/h, as shown in Figure 22.

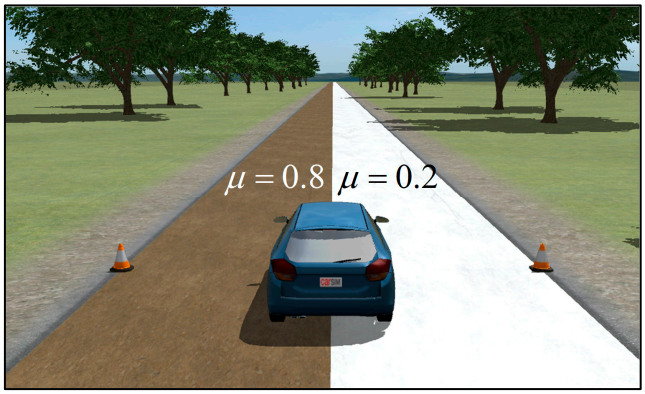

Figure 22. Simulation on a split road.

The vehicle is accelerated on the set split road, and the simulation results are shown in Figure 23:

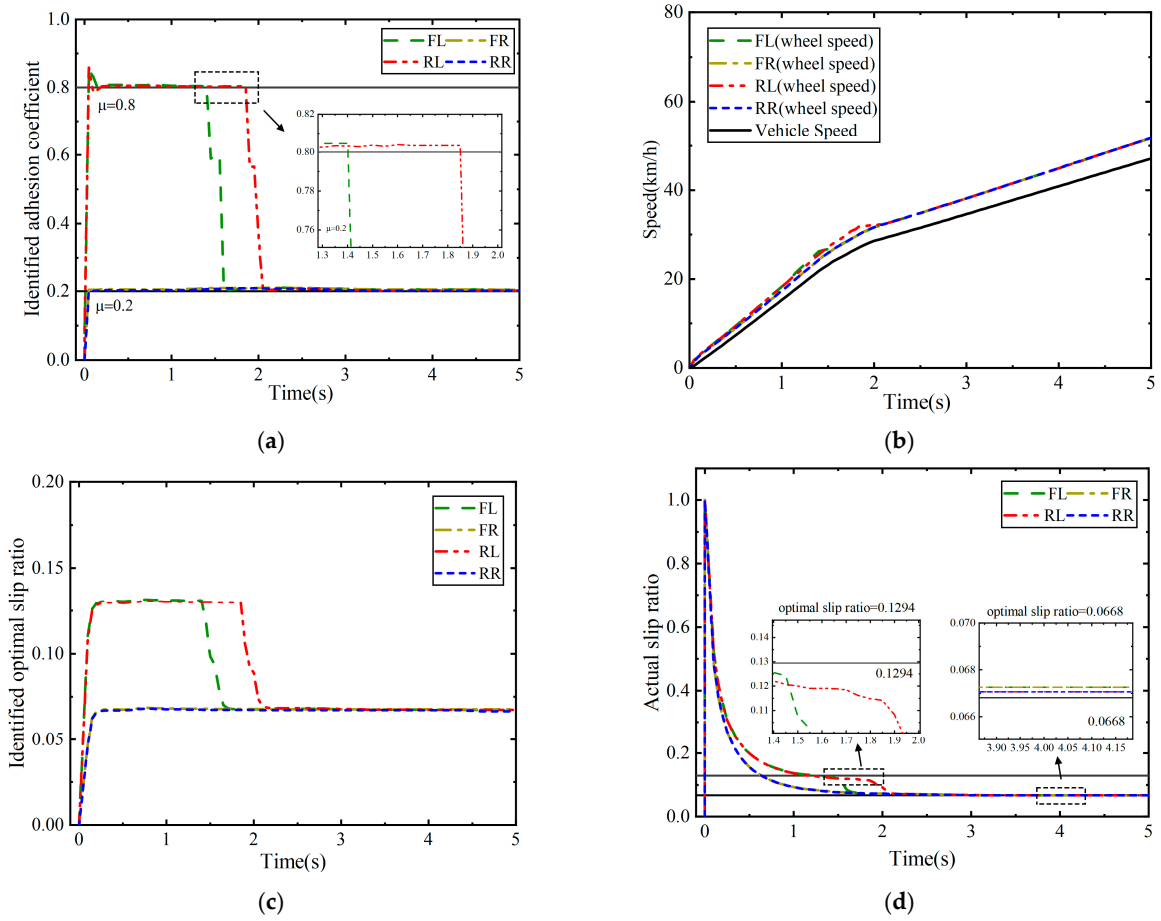

Figure 23. Simulation results of a split road: (**a**) Identified adhesion coefficient; (**b**) Wheel speed; (**c**) Identified optimal slip ratio; (**d**) Actual slip ratio.

When the vehicle starts on the split road surface, due to the different adhesion coefficients of the left and right wheels, each wheel accelerates at different rates. After 0.8 s, the

adhesion coefficient of the left front wheel stabilizes at 0.804 with an error of 0.004, the left rear wheel stabilizes at 0.802 with an error of 0.002; the right front wheel stabilizes at 0.205 with an error of 0.005, and the right rear wheel stabilizes at 0.202 with an error of 0.002. The slip ratio of the right front wheel is 0.0672 with an error of 0.0004, and the right rear wheel slip ratio is 0.067 with an error of 0.0002. The simulation results are summarized in Table 8.

Table 8. Results of the split road.

Optimal Slip Ratio = 0.0668		
	FR-Wheel	RR-Wheel
Actual slip ratio	0.0672	0.067
Absolute Error	0.0004	0.0002

However, during the simulation, it was found that the recognition results of the left wheels suddenly dropped, which can be attributed to the large difference in road conditions between the left and right sides, resulting in a large yaw moment during start-up and causing the vehicle to deviate from the track. The results of the vehicle yaw rate are shown in Figure 24.

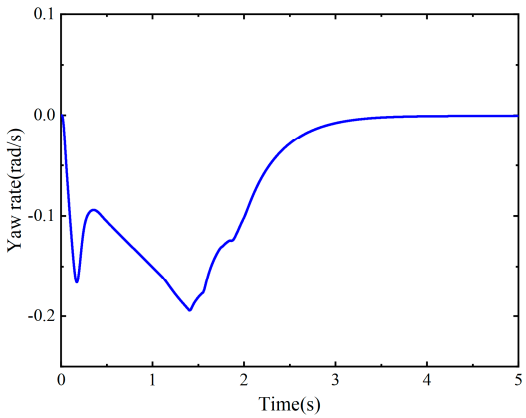

Figure 24. Yaw rate of the vehicle.

Due to the significant difference in the adhesion coefficients of the split road surface, there is a large torque difference between the two sides, resulting in a high yaw rate, causing the vehicle to deviate from its path. Once the vehicle fully transitions to the low-adhesion surface, the yaw rate drops to zero.

To address this issue, a torque distribution adjustment is implemented. When a large difference in adhesion coefficients between the left and right sides is detected, the lowest distribution principle is applied. Specifically, when the adhesion coefficient on the left side is greater than that on the right side, the left-side torque is adjusted to match the right-side torque. The simulation results are shown in Figure 25, where the torque distribution adjustment takes effect at 1 s.

Due to differing adhesion coefficients, the left wheels start with a coefficient of 0.8, while the right wheels start with 0.2, generating a yaw rate. Before the adjustment activates at 1 s, the yaw rate increases. After applying the lowest torque output principle due to the adhesion difference, the left front wheel's torque decreases, and the yaw rate approaches zero. The slip ratio remains low due to the use of low-adhesion torque on the high-adhesion surface. To verify the robustness of the proposed drive anti-slip controller, a comparison with a conventional sliding mode controller is performed (left front wheel as an example). The results are shown in Figure 26.

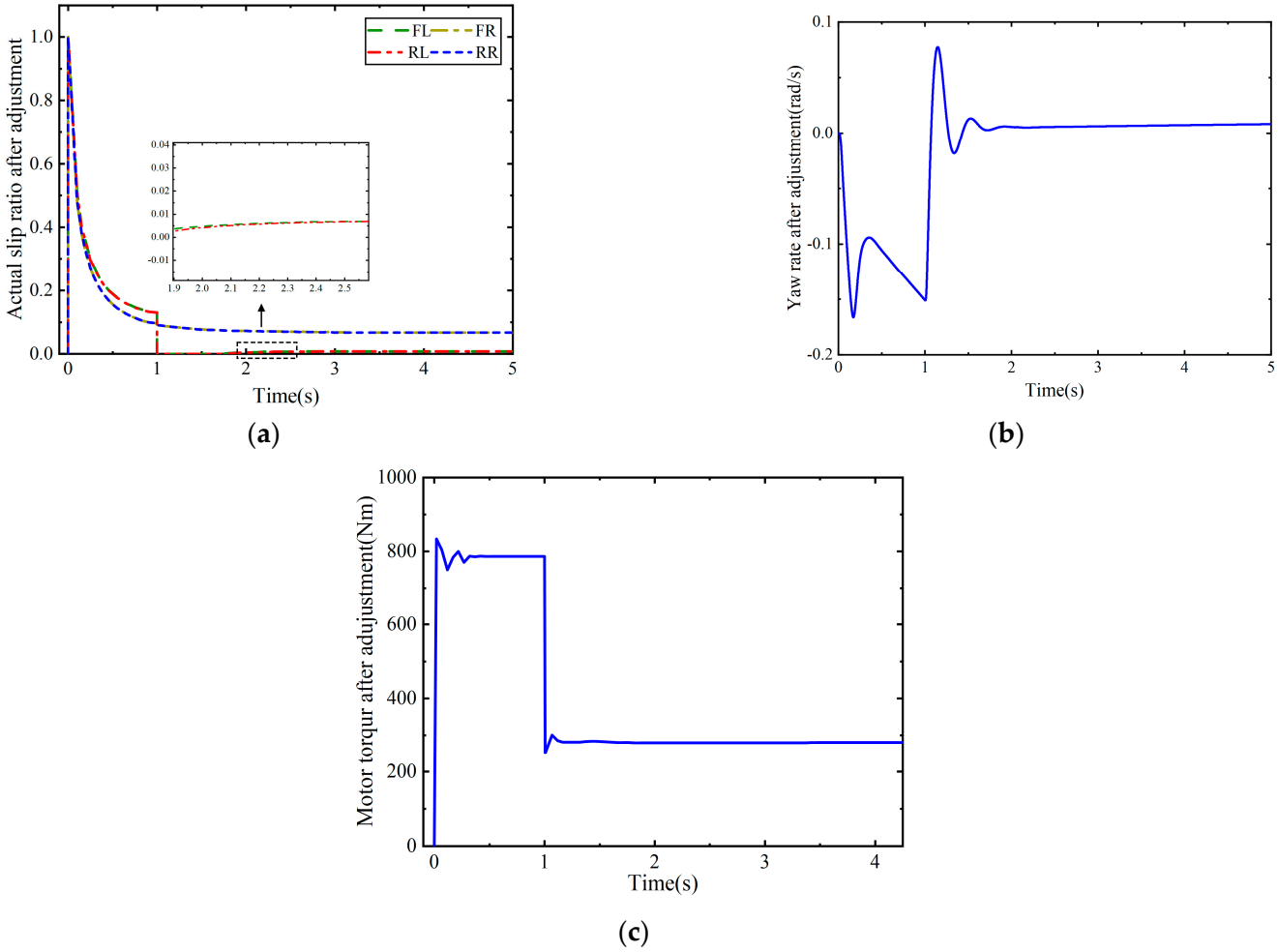

Figure 25. Simulation results after adjustment: (**a**) Actual slip ratio after adjustment; (**b**) Yaw rate after adjustment; (**c**) Motor torque after adjustment.

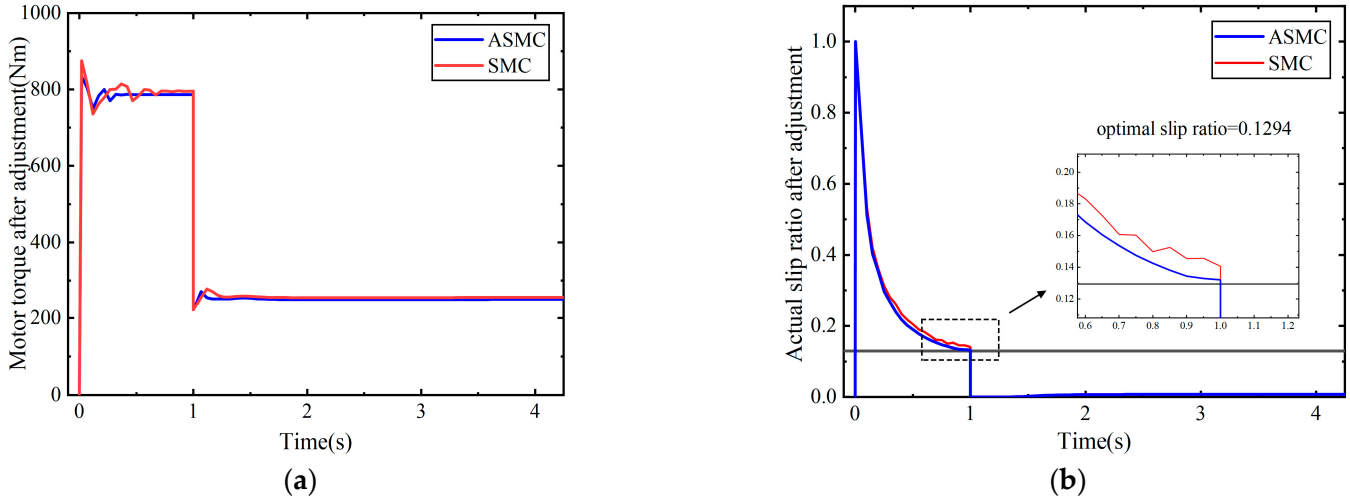

Figure 26. Comparison of different controllers on a split road: (**a**) Torque control comparison; (**b**) Slip ratio control comparison.

As shown in Figure 26a, under different control strategies, the output torque increases rapidly during acceleration. The improved ASMC quickly converges to a steady-state value, while the SMC exhibits oscillations and converges more slowly. After 1 s, the adjustment

strategy takes effect, and both strategies stabilize at lower torque outputs. The simulation results are summarized in Table 9.

Table 9. Comparison results of different algorithms of the split road.

	At 1 s	
	ASMC	SMC
Motor Torque (Nm)	786.4	796.2
Actual slip ratio	0.132	0.1407
Absolute Error	0.0026	0.0113
	After 1 s	
	ASMC	SMC
Motor Torque (Nm)	250.2	255.5
Actual slip ratio	0.00703	0.00781

As shown in Figure 26b, in this scenario, when the slip ratio has not fully converged and the distribution strategy is executed, the slip ratios are maintained at a relatively low level, meaning that the low-adhesion optimal torque control is executed on the high-adhesion surface. It can be observed that under SMC, there is a certain level of oscillation and error. The improved ASMC achieves better control performance.

5. Conclusions

This paper establishes a vehicle dynamics and Dugoff tire model, using an unscented Kalman filter to estimate the longitudinal speed with parameters from Carsim. Fuzzy control based on the Burckhardt tire model is implemented, with peak adhesion and optimal slip ratio curves fitted via a particle swarm-optimized BP neural network. An improved adaptive sliding mode controller optimizes torque distribution on split roads. Simulation results confirm the effectiveness of the approach.

On low-adhesion, jointed, and split roads, the proposed optimal slip ratio identification algorithm accurately identifies the road's optimal slip ratio, featuring fast response and high adaptability.

The improved adaptive sliding mode ASR controller demonstrates high accuracy, fast convergence, and strong robustness, effectively tracking optimal slip ratios and improving acceleration on various road surfaces. Compared to standard SMC, it reduces chattering, improves stability, and enhances response time and tracking precision.

In split road simulations, solely pursuing optimal slip ratios for each side increases the yaw rate and causes vehicle deviation. The proposed torque distribution strategy effectively mitigates this, ensuring stable straight-line driving with minimal yaw rate.

This study is primarily based on theoretical simulations. In practical applications, multiple factors may affect control performance. For example, sensor noise can impact vehicle speed estimation and slip ratio calculation, complex road conditions can increase the difficulty of road surface recognition, and the computational burden of the controller can affect accuracy. Additionally, the simplifications made in the model can be further explored in future research. For instance, road gradients, especially in steep conditions, can significantly impact the vehicle's center of gravity transfer and acceleration/deceleration, affecting road surface recognition. Air resistance can have a significant impact on vehicle speed and energy consumption at high speeds, and suspension damping is an important factor in analyzing vehicle stability and comfort. Future work could focus on adjusting control strategies qualitatively and quantitatively based on these factors, which would be of great value. To address these issues, real vehicle tests with signal filtering and experiments under various operating conditions are needed, along with the selection of appropriate hardware (Hall effect wheel speed sensors for accurate feedback), testing on surfaces with different friction coefficients, and testing at higher target speeds. Finally, adjusting controller parameters will help improve vehicle acceleration performance. Conducting and

furthering the above-mentioned future work will be highly valuable for deepening and broadening this study.

Author Contributions: Conceptualization, H.Z.; Methodology, H.Z. and Y.Q.; Software, Y.Q.; Validation, Y.Q.; Formal analysis, Y.Q., W.S. and C.Z.; Investigation, C.Z.; Data curation, W.S.; Writing—original draft, Y.Q.; Writing—review & editing, Y.Q.; Supervision, H.Z.; Project administration, H.Z. All authors have read and agreed to the published version of the manuscript.

Funding: This research received no external funding.

Data Availability Statement: Data are contained within the article.

Conflicts of Interest: The authors declare no conflict of interest.

References

1. Needell, Z.A.; McNerney, J.; Chang, M.T.; Trancik, J.E. Potential for widespread electrification of personal vehicle travel in the United States. *Nat. Energy* **2016**, *1*, 16112. [CrossRef]
2. Zhang, H. Technical progress and development trend of electric vehicles. In Proceedings of the 2017 International Conference on Innovations in Economic Management and Social Science (IEMSS 2017), Hangzhou, China, 15–16 April 2017; pp. 1415–1419.
3. Zhao, W.; Song, Q.; Liu, W.; Ahmad, M.; Li, Y. Distributed electric powertrain test bench with dynamic load controlled by neuron PI speed-tracking method. *IEEE Trans. Transp. Electrif.* **2019**, *5*, 433–443. [CrossRef]
4. Heydari, S.; Fajri, P.; Rasheduzzaman, M.; Sabzehgar, R. Maximizing regenerative braking energy recovery of electric vehicles through dynamic low-speed cutoff point detection. *IEEE Trans. Transp. Electrif.* **2019**, *5*, 262–270. [CrossRef]
5. Chu, W.; Luo, Y.; Zhao, F.; Li, K. Driving torque coordination control of distributed drive electric vehicles. *Automot. Eng.* **2012**, *34*, 185–189.
6. Guo, L.; Xu, H.; Zou, J. Acceleration slip regulation control strategy for four-wheel independent drive electric vehicles. *IEEJ Trans. Electr. Electron. Eng.* **2019**, *14*, 630–639. [CrossRef]
7. Liang, J.; Lu, Y.; Yin, G.; Fang, Z.; Zhuang, W.; Ren, Y.; Xu, L.; Li, Y. A distributed integrated control architecture of AFS and DYC based on MAS for distributed drive electric vehicles. *IEEE Trans. Veh. Technol.* **2021**, *70*, 5565–5577. [CrossRef]
8. Liang, J.; Feng, J.; Fang, Z.; Lu, Y.; Yin, G.; Mao, X.; Wu, J.; Wang, F. An energy-oriented torque-vector control framework for distributed drive electric vehicles. *IEEE Trans. Transp. Electrif.* **2023**, *9*, 4014–4031. [CrossRef]
9. Zirek, A.; Onat, A. A novel anti-slip control approach for railway vehicles with traction based on adhesion estimation with swarm intelligence. *Railw. Eng. Sci.* **2020**, *28*, 346–364. [CrossRef]
10. Shi, Q.; Wang, M.; He, Z.; Yao, C.; Wei, Y.; He, L. A fuzzy-based sliding mode control approach for acceleration slip regulation of battery electric vehicle. *Chin. J. Mech. Eng.* **2022**, *35*, 72. [CrossRef]
11. Wang, Y.; Yuan, L.; Chen, H.; Du, P.; Lian, X. An anti-slip control strategy with modifying target and torque reallocation for heavy in-wheel motor vehicle. *Proc. Inst. Mech. Eng. Part D J. Automob. Eng.* **2022**, *236*, 2625–2644. [CrossRef]
12. Hongbo, W.; Chunyang, W.; Han, G.; Shihan, X. Vehicle traction force control based on the road adhesion coefficient estimation by FFUKF. *Chin. J. Theor. Appl. Mech.* **2022**, *54*, 1866–1879.
13. De Pinto, S.; Chatzikomis, C.; Sorniotti, A.; Mantriota, G. Comparison of traction controllers for electric vehicles with on-board drivetrains. *IEEE Trans. Veh. Technol.* **2017**, *66*, 6715–6727. [CrossRef]
14. Hori, Y.; Toyoda, Y.; Tsuruoka, Y. Traction control of electric vehicle: Basic experimental results using the test EV "UOT electric march". *IEEE Trans. Ind. Appl.* **1998**, *34*, 1131–1138. [CrossRef]
15. Yin, D.; Hori, Y. Traction control for EV based on maximum transmissible torque estimation. *Int. J. Intell. Transp. Syst. Res.* **2010**, *8*, 1–9. [CrossRef]
16. Zhang, L.; Li, L.; Qi, B.; Song, J.; Xu, H. Torque adaptive traction control for distributed drive electric vehicle. *J. Mech. Eng.* **2013**, *49*, 106–113. [CrossRef]
17. Colli, V.; Tomassi, G.; Scarano, M. "Single Wheel" longitudinal traction control for electric vehicles. *IEEE Trans. Power Electron.* **2006**, *21*, 799–808. [CrossRef]
18. Deur, J.; Pavković, D.; Burgio, G.; Hrovat, D. A model-based traction control strategy non-reliant on wheel slip information. *Veh. Syst. Dyn.* **2011**, *49*, 1245–1265. [CrossRef]
19. Lipeng, Z.; Shuaishuai, L.; Haojie, Y.; Changan, R.; Shaohua, L. Centralized and distributed coupling traction control of electric vehicles on split ramps. *Mech. Mach. Theory* **2023**, *179*, 105098. [CrossRef]
20. Chen, G.; He, L.; Zhang, B.; Hua, M. Dynamics integrated control for four-wheel independent control electric vehicle. *Int. J. Heavy Veh. Syst.* **2019**, *26*, 515–534. [CrossRef]
21. Yang, G.; Li, J.; Fu, Z.; Fang, L. Optimization of logic threshold control strategy for electric vehicles with hybrid energy storage system by pseudo-spectral method. *Energy Procedia* **2018**, *152*, 508–513. [CrossRef]
22. Jun, L.; Yanzhao, S.; Hanbing, W. A research on the acceleration slip regulation strategy for a four wheel drive hybrid electric vehicle. *Automot. Eng.* **2017**, *39*, 296–303.

23. Sekour, M.h.; Hartani, K.; Merah, A. Electric vehicle longitudinal stability control based on a new multimachine nonlinear model predictive direct torque control. *J. Adv. Transp.* **2017**, *2017*, 4125384. [CrossRef]
24. Zhou, L.; Xiong, L.; Yu, Z.P. A research on Anti-slip regulation for 4WD electric vehicle with In-wheel motors. *Appl. Mech. Mater.* **2013**, *347*, 753–757. [CrossRef]
25. De Castro, R.; Araújo, R.E.; Freitas, D. Wheel slip control of EVs based on sliding mode technique with conditional integrators. *IEEE Trans. Ind. Electron.* **2012**, *60*, 3256–3271. [CrossRef]
26. Yu, Z.; Zhang, R.; Lu, X.; Jin, C.; Sun, K. Robust adaptive anti-slip regulation controller for a distributed-drive electric vehicle considering the driver's intended driving torque. *Proc. Inst. Mech. Eng. Part D J. Automob. Eng.* **2018**, *232*, 562–576. [CrossRef]
27. Zhang, Z.; Liu, C.-g.; Ma, X.-j.; Zhang, Y.-y.; Chen, L.-m. Driving force coordinated control of an 8 × 8 in-wheel motor drive vehicle with tire-road friction coefficient identification. *Def. Technol.* **2022**, *18*, 119–132. [CrossRef]
28. Wang, Z.; Ding, X.; Zhang, L. Chassis coordinated control for full x-by-wire four-wheel-independent-drive electric vehicles. *IEEE Trans. Veh. Technol.* **2022**, *72*, 4394–4410. [CrossRef]
29. Jagt, P.v.d.; Parsons, A. Road surface correction of tire test data. *Veh. Syst. Dyn.* **1996**, *25*, 147–165. [CrossRef]
30. Dugoff, H.; Fancher, P.S.; Segel, L. An analysis of tire traction properties and their influence on vehicle dynamic performance. *SAE Trans.* **1970**, *79*, 1219–1243.
31. Burckhardt, M. Wheel Slip Control Systems. 1993. Available online: https://scholar.google.com/scholar?hl=zh-CN&as_sdt=0,5&q=Burckhardt,+M.+Wheel+slip+control+systems.+1993.+&btnG= (accessed on 13 October 2024).
32. Li, B.; Xiong, L.; Leng, B. Adaptive anti-slip regulation method for electric vehicle with in-wheel motors considering the road slope. In Proceedings of the 2018 IEEE Intelligent Vehicles Symposium (IV), Changshu, China, 26–30 June 2018; pp. 1–6.
33. Li, Y.; Li, J.; Huang, J.; Zhou, H. Fitting analysis and research of measured data of SAW micro-pressure sensor based on BP neural network. *Measurement* **2020**, *155*, 107533. [CrossRef]

Disclaimer/Publisher's Note: The statements, opinions and data contained in all publications are solely those of the individual author(s) and contributor(s) and not of MDPI and/or the editor(s). MDPI and/or the editor(s) disclaim responsibility for any injury to people or property resulting from any ideas, methods, instructions or products referred to in the content.